












GSED: The Galactic Stellar Extinction Database

BAISONG ZHANG ¹, BINGQIU CHEN ¹, DONGWEI FAN ^{1,2,3}, HAIBO YUAN ^{4,5}, PINJIAN CHEN ^{2,6}, HELONG GUO ^{7,8},
LIN ZHANG ¹, BAOKUN SUN ⁹, XINGZHU ZOU ¹, LUNWEI ZHANG ¹⁰, YANAN CAO,¹ AND LONGFEI DING ¹

¹*South-Western Institute for Astronomy Research, Yunnan University, Kunming, Yunnan 650091, China*

²*National Astronomical Observatories, Chinese Academy of Sciences, Beijing 100101, China*

³*National Astronomical Data Center, Beijing 100101, China*

⁴*School of Physics and Astronomy, Beijing Normal University, Beijing 100875, China*

⁵*Institute for Frontiers in Astronomy and Astrophysics, Beijing Normal University, Beijing 102206, China*

⁶*School of Astronomy and Space Science, University of the Chinese Academy of Sciences, Beijing, 100049, China*

⁷*Research Center of Astronomy, QingHai University, Xining, 810016, China*

⁸*Department of Physics and Astronomy, QingHai University, Xining, 810016, China*

⁹*Institute of Astrophysics, Chuxiong Normal College, Chuxiong 675000, China*

¹⁰*School of Mathematics, Physics and Statistics, Honghe University, Mengzi, Yunnan 661100, China*

ABSTRACT

Reliable extinction correction is essential for nearly all astrophysical studies within the Galaxy. We present the Galactic Stellar Extinction Database (GSED, <https://nadc.china-vo.org/data/gsed/>), a homogenised database that unifies six representative 3D extinction datasets under a common $E(B-V)$ and parallax-distance baseline. A six-layer multilayer perceptron is designed to correct the systematic differences in both extinction and distance across the heterogeneous input catalogues. Applying the trained models yields a catalogue of over 1.9 billion homogenised entries, which is built into a publicly accessible, real-time query service: a user supplies a coordinate and a search radius, the system retrieves the data, fits the distance–extinction relation, returns $E(B-V)$ together with $E(G_{BP} - G_{RP})$ and A_V , and allows the raw catalogue and the fitted curve to be downloaded. By delivering extinction as raw stellar measurements rather than voxelised map products and retaining the capacity to incorporate future datasets, GSED provides a flexible, traceable, and extensible new tool for Galactic extinction correction and dust-structure studies.

Keywords: Milky Way Galaxy(1054); Interstellar dust extinction (837); Interstellar extinction (841); Interstellar reddening (853)

1. INTRODUCTION

Nearly a century ago, Trumpler (1930) established through studies of Galactic star clusters that interstellar dust is ubiquitous and dims and reddens background objects. Dust causes extinction and reddening in the ultraviolet, optical, and near-infrared through absorption and scattering, and it constitutes a foreground contamination that almost every relevant observation

must confront (Draine 2003). To recover the luminosity and colour of an object, and thereby to assess its intrinsic properties and physical parameters accurately, the extinction and reddening of dust must be removed. Whether a reliable extinction estimate can be obtained for an arbitrary object or line of sight therefore often determines the precision of the associated study directly.

Such extinction information has long come mainly from extinction maps that describe the spatial distribution of dust. Depending on whether distance information is included, extinction maps fall into two-dimensional (2D) and three-dimensional (3D) classes. 2D extinction maps (e.g. Schlegel et al. 1998; Schultheis et al. 1999; Gonzalez et al. 2012; Planck Collaboration et al. 2014; Gontcharov et al. 2025), provide the cumu-

Corresponding author: Bingqiu Chen
bchen@ynu.edu.cn

Corresponding author: Dongwei Fan
fandongwei@nao.cas.cn

lative total extinction along the line of sight and cannot distinguish dust at different distances, so they tend to overestimate the actual extinction of disc stars embedded within the dust layer (Berry et al. 2012; Chen et al. 2014). 3D extinction maps add the crucial distance dimension and depict the 3D structure of interstellar dust more accurately, which makes them a focus of recent research, and we list only a few representative works here. Early 3D maps relied mainly on photometric or model-dependent distance estimates and thus achieved limited distance precision. Marshall et al. (2006) construct a 3D extinction map of the inner Galactic disc ($|l| \leq 100^\circ$, $|b| \leq 10^\circ$), Chen et al. (2013) and Schultheis et al. (2014) construct 3D maps of the Galactic bulge region, Chen et al. (2014) construct a 3D map toward the anticentre ($140^\circ < l < 240^\circ$, $-60^\circ < b < 40^\circ$), and Hanson et al. (2016) construct a 3D map near the Galactic plane ($0^\circ < l < 250^\circ$, $|b| < 4.5^\circ$). After the release of the Gaia data (Gaia Collaboration et al. 2018), high-precision trigonometric parallaxes greatly improved the precision of stellar distances and gave rise to a series of 3D maps with higher distance accuracy. Chen et al. (2019), hereafter Chen19, use Gaia DR2 and the Two Micron All Sky Survey (2MASS; Skrutskie et al. 2006) photometry to cover the entire Galactic disc ($0^\circ < l < 360^\circ$, $|b| < 10^\circ$); Green et al. (2019), hereafter Green19, use Gaia DR2, Pan-STARRS1 (Chambers et al. 2016), and 2MASS to construct a 3D map covering $\delta > -30^\circ$; Guo et al. (2021), hereafter Guo21, use SkyMapper (Wolf et al. 2018), Gaia DR2, and 2MASS to construct a 3D map of the southern sky; and Zucker et al. (2025), hereafter Zucker25, use deep photometry from the Dark Energy Camera Plane Survey 2 (DECaPS2; Saydjari et al. 2023) to construct a map of the southern Galactic disc ($239^\circ < l < 6^\circ$, $|b| < 10^\circ$). Wang et al. (2025) provide an all-sky 3D map based on Gaia XP (Zhang et al. 2023; Zhang & Green 2025) and the Large Sky Area Multi-Object Fiber Spectroscopic Telescope (LAMOST; Zhao et al. (2012)) data.

With these maps in hand, objects within the Galaxy can be corrected using extinction-correction tools, among which Dustmaps (Green 2018) and GALExtin (Amôres et al. 2021) are the most widely used. Dustmaps integrates a variety of extinction maps into a single query interface within a unified framework, supporting the 2D maps of Schlegel et al. (1998) and Planck Collaboration et al. (2014) together with the 3D maps of Marshall et al. (2006), Chen et al. (2014), Green et al. (2015, 2018, 2019), Edenhofer et al. (2024), and Zucker et al. (2025), etc., from which users may select as needed and call through the common interface. GALExtin is an online tool designed specifically for extinction correction

that integrates multiple maps through a web interface in an intuitive and convenient manner. Beyond these two comprehensive tools, some authors also provide dedicated query sites or programs for their own maps, such as Guo et al. (2021), who release extinction-correction tools for the southern and all-sky regions based on the Dustmaps framework, and Wang et al. (2025), who also provide an online site for querying their all-sky map.

Although these tools offer important computational interfaces, three limitations remain difficult to avoid in practice. The first is the fragmentation of coverage. As noted above, a single extinction map often covers only a specific region or a specific distance range, so the maps complement one another yet do not connect. With both Dustmaps and GALExtin, users must specify the map in advance and be familiar with its coverage boundaries, and once a target source lies at the edge of a map or beyond its coverage, obtaining a valid or reliable extinction estimate becomes difficult, which raises the threshold for use. The second is the lack of a common calibration baseline together with the presence of systematic differences. Different maps adopt different extinction tracers such as $E(B - V)$, $E(g - r)$, A_r , and A_V , different distance scales, and different inversion methods and priors, and therefore carry non-negligible systematic differences among one another. Directly stitching them together or converting between them with fixed extinction coefficients introduces clear biases and seams into the result, so they cannot simply be merged into a single homogeneous all-sky map. The third is the absence of raw information and insufficient flexibility. Existing tools return only the extinction value at one point and at one fixed resolution, without providing the raw stellar sample along that line of sight; the window used to fit the distance-extinction relation is fixed in advance, so a reliable estimate cannot be obtained where the data are sparse, while lowering the resolution in exchange for more data introduces bias, and users cannot redo the fit from the raw data themselves. In addition, Dustmaps requires the large volume of extinction data to be downloaded locally before use.

To address these shortcomings, we construct the Galactic Stellar Extinction Database (GSED). Unlike redrawing another extinction map, GSED stores the extinction and distance measurements of roughly 1.936 billion individual stars. We adopt the accurate colour excess $E(B - V)$ of Wang et al. (2025) and the parallax distances of Zhang & Green (2025, hereafter Zhang25) as a common baseline, normalising the extinction systematics and distance scales of six representative datasets onto a single system, thereby integrating data that were previously separate and disconnected into a homogeneous,

all-sky database whose components can speak to one another. Because the data are stored at the stellar level, GSED allows users to specify a query radius according to their needs in order to adjust the resolution of the extinction data dynamically, to obtain the raw stellar sample within the search region, and to obtain more accurate and traceable results in distance and extinction. Moreover, the systematic-correction and distance-correction framework of GSED can be reused for extinction datasets released in the future, giving the database the capacity to expand continuously, with its data volume and coverage growing as subsequent surveys advance.

2. DATA

As the first version of the GSED database, we select six recently published and representative large catalogues of stellar distances and extinction. We note that we do not include every published work of this kind; the design of GSED allows new extinction data to be incorporated continuously, and other extinction catalogues, for example Yu et al. (2026), will be added in due course.

Chen19 uses the photometry and astrometry of Gaia DR2 together with near-infrared photometry and applies a random forest machine learning method to obtain the $E(G_{\text{BP}} - G_{\text{RP}})$ reddening of about 56 million stars; after removing stars with large parallax errors in Gaia DR2, the work provides extinction and distance information for more than 35 million stars covering the disc region $0^\circ < l < 360^\circ$, $|b| < 10^\circ$. Green19 uses multi-band photometry from Gaia DR2, Pan-STARRS1, and 2MASS and applies a Bayesian method to infer stellar atmospheric parameters, distance, and extinction simultaneously, providing the reddening and distance of about 799 million stars covering $\delta > -30^\circ$. Guo21 combines multi-band data from SkyMapper, Gaia DR2, and near-infrared photometry and derives reliable A_r extinction and distances for about 19 million stars within roughly $14,000 \text{ deg}^2$ of the southern sky through SED fitting. Sun et al. (2025), hereafter Sun25, uses data including SkyMapper and Gaia and obtains the stellar parameters, $E(BP - RP)$ reddening, and distances of about 140 million southern-sky stars through the SPAr method (Sun et al. 2023). Zucker25 uses deep photometry including the Dark Energy Camera Plane Survey 2 (DECaPS2; Saydjari et al. 2023) together with Gaia DR3 parallaxes and applies the brutus stellar-parameter inference framework to give the A_V extinction and distances of about 700 million stars in the southern Galactic disc ($239^\circ < l < 6^\circ$, $|b| < 10^\circ$). Zhang25 uses Gaia XP low-resolution spectra and near-infrared photometry such as 2MASS to develop a data-driven forward model

and measures the extinction curve $R(V)$, $E(B - V)$, stellar parameters, and distances of about 130 million high-quality stars covering the whole sky.

These six datasets differ in their extinction tracers, distance scales, and stellar-parameter spaces. To calibrate them onto a single system, we prepare MLP inputs for each dataset. The atmospheric parameters or intrinsic colour are the feature inputs required by the MLP model to learn the extinction systematics, as described in Section 3. Because the catalogues provide different raw information, we need to fill in the missing parameters.

Chen19 and Guo21 compute only the stellar extinction, adopt the Gaia DR2 parallax distance, and do not provide T_{eff} or $[\text{Fe}/\text{H}]$, so the intrinsic colour must be derived from Gaia DR3 colours as a substitute input. We therefore cross-match Chen19 and Guo21 with Gaia DR3 (Gaia Collaboration et al. 2023) within a radius of 1 arcsec to obtain the Gaia DR3 parallaxes and the $G_{\text{BP}} - G_{\text{RP}}$ colour, hereafter $BP - RP$, and we remove entries with null parallax or $BP - RP$ colour. We also impose the following constraints on the parallaxes: $\text{Plx} > 0.02$, $\text{e_Plx} > 0$, and $\text{e_Plx} / \text{Plx} < 0.5$. The distance d and distance error d_{err} of Chen19 and Guo21 follow directly from the parallaxes. From the Gaia DR3 $BP - RP$ colour and the extinction of Chen19 and Guo21, combined with the extinction law given by Chen19, we further obtain the intrinsic colour $(BP - RP)_0$ of each star. For Green19, we cross-match its data with Pan-STARRS1 within a radius of 1 arcsec to obtain the g - and r -band photometry, and after removing null values we derive the intrinsic colour $(g - r)_0$ using the extinction $E(g - r)$. For Sun25, Zucker25, and Zhang25, the catalogues already provide atmospheric parameters such as T_{eff} and $[\text{Fe}/\text{H}]$ directly, which serve as input features of the MLP model without additional cross-matching.

3. CORRECTION OF EXTINCTION AND DISTANCE SYSTEMATICS

As described in Section 2, the six extinction datasets differ in their extinction tracers, distance scales, and stellar-parameter spaces and cannot be merged directly. To calibrate them into a single system, we select a reasonable reference baseline. For extinction, we adopt the colour excess $E(B - V)$ of Wang et al. (2025) as the baseline. The extinction catalogue of Wang et al. (2025) is based on the parameters of A-, F-, G-, and K-type stars in the LAMOST DR11 v1.0 low-resolution spectroscopic survey and applies the standard-pair method (Yuan et al. 2013) to obtain the extinction of about 4.6 million independent sources. This catalogue has a typi-

cal precision of about 0.02 mag and is currently the spectroscopic extinction catalogue with the highest precision and the largest sample. For distance, we adopt the parallax distances of the Zhang25 catalogue as the baseline. Based on Gaia trigonometric parallaxes and processed with strict quality selection and a forward model, that catalogue provides a high-precision and self-consistent distance scale covering the whole sky. On this baseline, we design a unified six-layer MLP framework that takes the raw extinction and distance of each catalogue as the main inputs, supplemented by auxiliary features such as atmospheric parameters, intrinsic colour, or position, and uses the baseline $E(B - V)$ and the baseline distance as supervision values to learn the complex relations between each dataset and the baseline through a mapping in a high-dimensional feature space, thereby correcting the extinction and distance systematics in a unified manner.

3.1. Correction of Extinction Systematics

The systematic differences among extinction datasets arise mainly from two sources. The first is the different stellar intrinsic colours or atmospheric parameters adopted, which lead to differences in the extinction zero point. The second is the different extinction laws assumed and extinction coefficients used, since the extinction coefficient itself varies with stellar effective temperature and extinction (Shen et al. 2022; Zhang & Yuan 2023), so that the conversion between the same extinction tracers differs from one work to another. The extinction systematics therefore change with stellar spectral type and metallicity and also depend on the magnitude of the extinction itself, and they cannot be corrected by a single fixed scaling factor. Based on this understanding, we use the raw extinction together with the atmospheric parameters or intrinsic colour as the input features of the MLP, so that the model can learn how the extinction bias varies with stellar parameters. The specific choice of inputs is also constrained by the information each catalogue provides. For the catalogues that supply T_{eff} and $[\text{Fe}/\text{H}]$, namely Sun25, Zucker25, and Zhang25, we use these two parameters directly; for the catalogues without an effective temperature, we adopt the stellar intrinsic colour as a proxy for spectral type, with Chen19 and Guo21 providing $(BP - RP)_0$ and Green19 providing $(g - r)_0$; and since Green19 additionally provides $[\text{Fe}/\text{H}]$, we include it as well.

Fig. 1 shows the architecture of the deep neural network proposed in this work. It adopts a fully connected design and comprises an input layer, five hidden layers, and one output layer for a total of six layers, with a fixed hidden width of 128 dimensions, ReLU activa-

Table 1. Input parameters and loss results of the extinction-systematics correction models for the different catalogues.

Source	Input Parameters	Loss (MAE)
Chen19	$E(BP - RP), (BP - RP)_0$	0.0541
Green19	$E, (g - r)_0, [\text{Fe}/\text{H}]$	0.0632
Guo21	$A_r, (BP - RP)_0$	0.0326
Sun25	$E(BP - RP), T_{\text{eff}}, [\text{Fe}/\text{H}]$	0.0255
Zhang25	$E, T_{\text{eff}}, [\text{Fe}/\text{H}]$	0.0211
Zucker25	$A_V, T_{\text{eff}}, [\text{Fe}/\text{H}]$	0.0561

tion, and no activation in the output layer so as to preserve the continuity and dynamic range of the regression. The core logic of the network is to learn the systematic difference between the input extinction and the target baseline extinction through a mapping in a high-dimensional feature space. During training, the colour excess $E(B - V)$ of the Wang et al. (2025) extinction catalogue serves as the supervision value, and the model is optimised with an L1 loss, namely the mean absolute error (MAE),

$$\mathcal{L} = \frac{1}{N} \sum_{i=1}^N |E(B - V)_i^{\text{true}} - E(B - V)_i^{\text{model}}|, \quad (1)$$

where N is the total number of samples and $E(B - V)_i^{\text{true}}$ and $E(B - V)_i^{\text{model}}$ denote the target extinction and the model prediction for the i -th star. We use the MAE because its error term grows linearly and is insensitive to outliers, so it remains robust when the data contain many points with large scatter.

Each of the six extinction datasets is cross-matched with the Wang et al. catalogue, and an MLP model of identical structure is trained separately. The input parameters, data selection, and detailed results of each model are given in Appendix A, and the overall performance is summarised here. Table 1 summarises the input parameters and the test-set performance of the extinction-systematics correction models, all of which use the same learning rate of 2.0×10^{-2} . The Chen19 and Guo21 models take the extinction and $(BP - RP)_0$ as inputs and achieve test-set losses of 0.0541 and 0.0326, respectively; the Green19 model takes the extinction, $(g - r)_0$, and $[\text{Fe}/\text{H}]$ as inputs and achieves a loss of 0.0632; and the Sun25, Zhang25, and Zucker25 models take the extinction, T_{eff} , and $[\text{Fe}/\text{H}]$ as inputs and achieve losses of 0.0255, 0.0211, and 0.0561, respectively.

The Zhang25 model achieves the smallest loss for two reasons: first, its extinction tracer E is almost the same as that of the Wang et al. baseline, so the two are already close; second, its measurements are derived from Gaia low-resolution spectroscopy, which yields in-

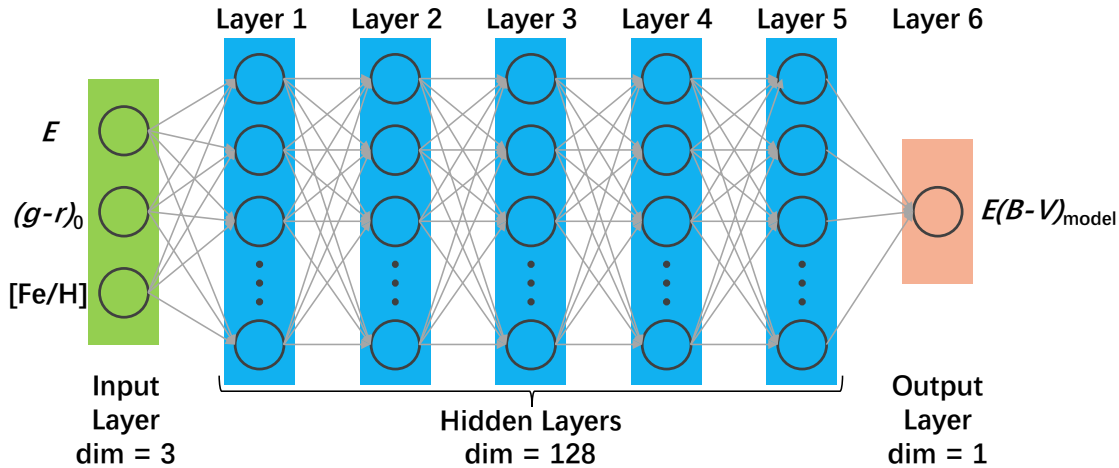


Figure 1. Network architecture of the extinction-systematics correction model. The input parameters differ slightly among works, and this figure takes the correction of the extinction systematics of Green et al. (2019) as an example.

herently higher precision than multi-band photometry. In contrast, Green19, Chen19, and Zucker25 provide broadband extinction or reddening in other passbands, and their measurements are based on multi-band photometry whose typical extinction uncertainty reaches 0.05–0.06 mag (Chen et al. 2015), introducing substantially larger scatter relative to the baseline. The losses of Guo21 and Sun25 are small, at 0.0326 and 0.0255, mainly because both are southern-sky data and their cross-matched samples with the Wang et al. catalogue, whose parent sample LAMOST covers mostly the northern sky, are relatively few; nevertheless, the number of matched samples remains sufficient and covers the necessary parameter space, so the model training remains effective. The figures in the appendix show that, for each dataset, the raw extinction carries a systematic difference that varies markedly with the atmospheric parameters and the extinction, and that after the MLP correction the residual between the corrected value and the baseline $E(B - V)_{\text{Wang25}}$ concentrates around zero and no longer shows any systematic trend with any parameter, indicating that the model removes the extinction systematics effectively. Furthermore, in Appendix C, we test whether the input parameter $[\text{Fe}/\text{H}]$ affects the results.

We note that the MLP essentially learns the average mapping between the input and the baseline, so its prediction represents the most probable baseline extinction under given input conditions rather than an exact reproduction of every data point. When the scatter between the raw extinction and the baseline is large and the correlation is weak, the prediction residual grows accordingly. In addition, the training is limited by the parameter-space coverage of the supervision sample, and since the Wang et al. (2025) catalogue matches few

Table 2. Input parameters and loss results of the distance-systematics correction models for the different catalogues.

Source	Input Parameters	Loss (MAE)
Chen19	l, b, D_{Chen19}	0.2132
Green19	l, b, D_{Green19}	0.1848
Guo21	l, b, D_{Guo21}	0.0397
Sun25	l, b, D_{Sun25}	0.5452
Zucker25	$l, b, D_{\text{Zucker25}}$	0.3860

training samples in the high-extinction regime, the generalisation of the model in those regions is somewhat reduced.

3.2. Correction of Distance Systematics

The differences in distance among catalogues arise mainly from two aspects. The first is the different distance-estimation methods, including photometric distances, trigonometric parallax distances, and their respective priors and processing pipelines, which may introduce a systematic zero-point offset. The second is the different sky coverage and detection depth of the surveys, so the distance systematics may vary with the line of sight. We therefore use the Galactic longitude l , the Galactic latitude b , and the raw distance d as the input features of the MLP, so that the model can learn how the distance bias varies with position and distance simultaneously. The distance-correction model adopts the same six-layer MLP structure as the extinction-correction model and differs only in its input features and supervision value, taking l, b , and the raw distance d as inputs and the distance D_{Zhang25} converted from parallax in the Zhang25 catalogue as the supervision value.

Five of the datasets, with Zhang25 itself serving as the distance baseline and requiring no calibration, are each cross-matched with the Zhang25 catalogue, and a MLP model of identical structure is trained separately. The input parameters, data selection and detailed results of each model are given in Appendix B, and the overall performance is summarised here. Table 2 summarises the input parameters and the test-set performance of the distance-correction models, all of which take the Galactic longitude l , the Galactic latitude b , and the distance D as inputs and use the same learning rate of 2.0×10^{-2} . The differences in the distance-correction performance among the models are closely tied to the characteristics of the data themselves. The Guo21 loss is the smallest at 0.0397, for three reasons: its total sample is small and its data quality is fairly uniform; limited by the sky coverage of the early SkyMapper data release, it contains few stars in the low-latitude, high-extinction, and high-density regions of the disc; and its stars are generally bright, so the Gaia trigonometric parallaxes are measured with high precision and the raw distances deviate little from the baseline.

The losses of Chen19, Green19, Sun25, and Zucker25 are relatively large, ranging from 0.18 to 0.55, for two reasons. First, a large fraction of the stars in these four datasets lie in the high-density regions of the disc, where the scatter of the Gaia trigonometric parallaxes increases markedly (Lindgren et al. 2021) and the raw distances are inherently uncertain. Second, Green19, Sun25, and Zucker25 all contain a considerable proportion of distant stars whose distances rely mainly on photometric parallaxes rather than Gaia trigonometric parallaxes and therefore carry large intrinsic errors. The Chen19 loss of 0.2132 is the smallest among the four, benefiting from its more conservative parallax-error selection, which removes stars with poor distance precision. In general, the clearer the trend and the smaller the scatter between the raw distance of a catalogue and the baseline distance, the better the model performs. The figures in the appendix likewise show that the raw distances carry a systematic bias that varies with the line of sight and the distance, and that after the MLP calibration the residual reaches zero with no systematic trend, which verifies the effectiveness of our distance systematics correction.

4. THE GALACTIC STELLAR EXTINCTION DATABASE

We apply the trained models to the raw data and obtain a catalogue in which the extinction and distance systematics are corrected. The catalogue contains 1,935,987,083 entries in total, and the number of ex-

Table 3. Statistics of the extinction data.

Source	Number
Chen19	50,712,371
Green19	798,990,486
Guo21	17,356,887
Sun25	140,599,779
Zucker25	709,129,917
Zhang25	219,197,643

inction entries from each work is summarised in Table 3. Fig. 2 shows the cumulative extinction sky maps of two distance ranges drawn from our catalogue on a HEALPix grid in Mollweide projection and Galactic coordinates. The data pass a quality selection of $d_err/d \leq 0.2$, $0 \leq E(B - V)_err \leq 0.1$, and $E(B - V) \geq 0$, and each pixel takes the inverse-variance-weighted mean $E(B - V)$.

At small distances we see many well-known local dust cloud structures, while at large distances the high-extinction regions concentrate near the Galactic plane. The maps are consistent with the known large-scale features of the dust distribution.

Storing such a large dataset and supporting real-time queries is a demanding task. For ease of use, we build the GSED with real-time query capability. The database holds eight columns of data, namely the right ascension (RA), declination (Dec), Galactic longitude (l), Galactic latitude (b), distance (d), distance error (d_err), extinction (e , i.e. $E(B - V)$), and extinction error (e_err , i.e. $E(B - V)_err$). We build the database system through a strategy of reuse and customisation to enable fast queries, with four specific optimisations. First, we reuse HEALPix spatial partitioning and a multi-level tree index to shard the roughly 1.936 billion extinction entries finely by sky region, so that a query locates only the target shards, which greatly reduces the scan range and accelerates the query. Second, we use a lightweight Python web framework that calls the encapsulated retrieval interface, data-parsing modules, and front-end display modules directly, integrating the data adaptation and the coordinate-system retrieval logic. Third, we reuse a coordinate-adaptation module to convert between the equatorial system, comprising RA and Dec, and the Galactic system, comprising l and b , and to retrieve data precisely. Fourth, we reuse an LRU (Least Recently Used) caching technique to keep frequently queried sky regions in memory, further improving the retrieval speed of the integrated multi-source data.

4.1. Distance-Extinction Curve Fitting

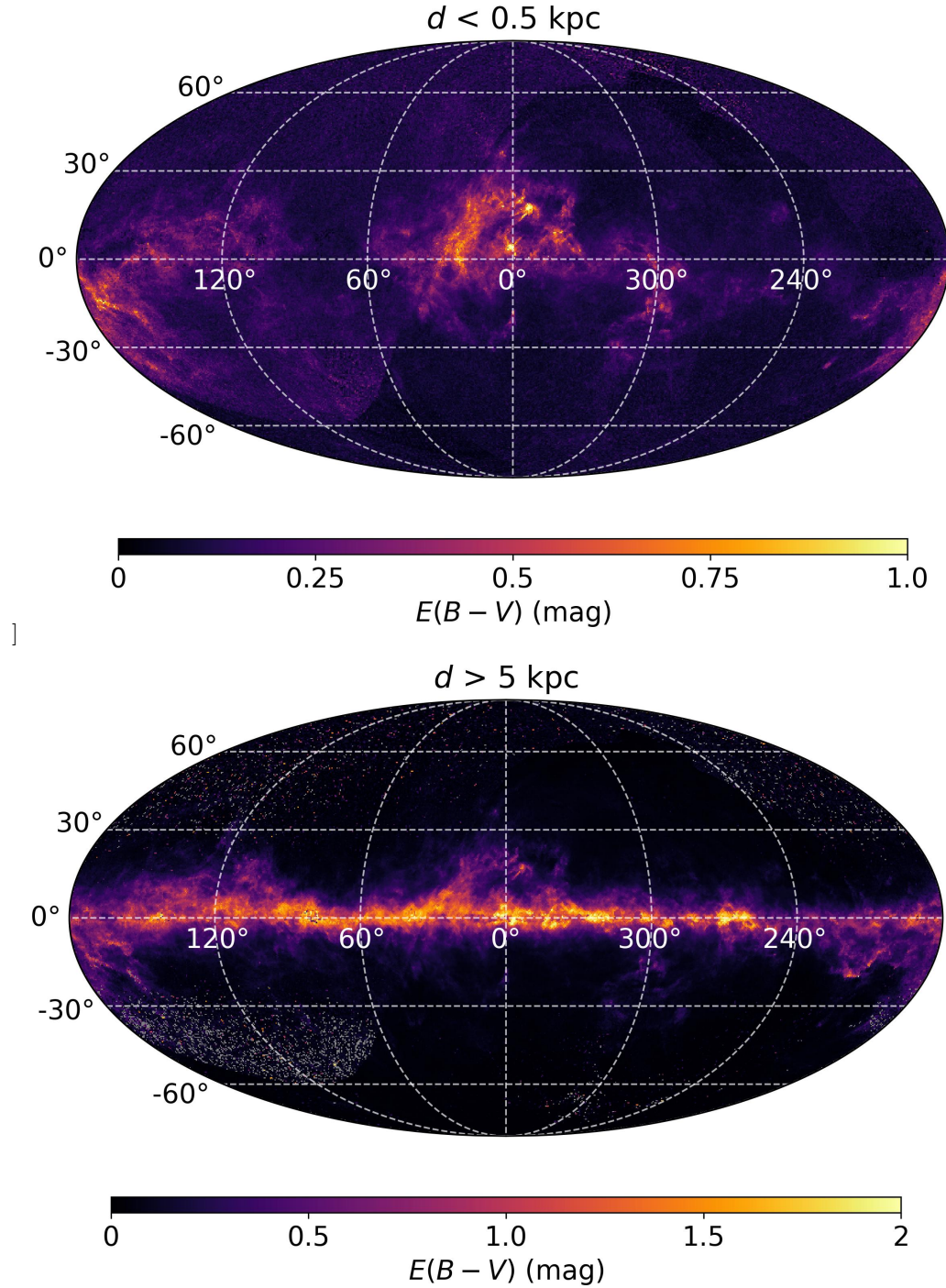


Figure 2. Cumulative $E(B - V)$ extinction sky maps in different distance intervals, shown in Galactic coordinates with a Mollweide projection. The two panels correspond to the ranges $d < 0.5$ kpc (upper) and $d > 5$ kpc (bottom). Each pixel takes the inverse-variance-weighted mean $E(B - V)$ of the valid samples within it, and the colour bar denotes $E(B - V)$ in mag. The data pass a quality selection of $d_{err}/d \leq 0.2$, $0 \leq E(B - V)_{err} \leq 0.1$, and $E(B - V) \geq 0$.

The GSED database stores the extinction and distance measurements of individual stars, whereas users usually need the extinction at a specific target distance along a given line of sight. We therefore provide the capability to fit the discrete stellar extinction–distance data points along a line of sight into a continuous extinction-growth curve $E(d)$ and then to interpolate or extrapolate the extinction at any distance.

Extinction is essentially the cumulative contribution of the interstellar medium along the line of sight, so the curve $E(d)$ must satisfy the physical constraint of monotonic increase. We accordingly divide the line of sight into k discrete distance intervals and parameterise the extinction increment of each interval as e^{h_i} , which is always positive, so that the cumulative extinction is $\sum_{i=0}^k e^{h_i}$ and $E(d)$ naturally increases monotonically with distance. For the fitting, we use MCMC sampling to explore the posterior probability of the parameters θ . Considering that the queried extinction data may contain a certain fraction of outliers, such as distance or extinction anomalies caused by stellar misclassification or parallax errors, we adopt a Cauchy-like log-likelihood to reduce the penalty weight of large-residual points,

$$\ln \mathcal{L} = - \sum_{i=1}^N \ln \left(1 + \left[\frac{E_i - f(d_i, \theta)}{\sigma E_i} \right]^2 \right), \quad (2)$$

where N is the number of valid samples and $f(d_i, \theta)$ is the cumulative extinction predicted by the model. Compared with the \mathcal{L}_2 norm, the logarithmic term $\ln(1 + r^2)$ grows slowly, allowing the model to tolerate outliers without being dominated by them and ensuring that the fitted curve captures the overall trend of the extinction. To improve the convergence efficiency of the MCMC sampling, we adopt a cooperative initialisation strategy, first performing a pre-fit with nonlinear least squares to locate the optimal parameter range quickly and then constructing the initial-state matrix of the Markov chain centred on this result, introducing a moderate random perturbation to increase the dispersion of the initial distribution so that the sampler reaches the global optimum efficiently.

4.2. Using the Database

To make these data easy to obtain, we develop a website accessible at <https://nadc.china-vo.org/data/gsed/> that aims to let users obtain extinction information quickly, as shown in Fig. 3. From the coordinate entered by the user, which can be switched between the equatorial and Galactic systems, the search radius, and the specified distance, the extinction data within this region are obtained, and the program decides whether to fit the distance–extinction curve according to the amount

Table 4. MCMC-fitted distance–extinction curve for the same line of sight as in Table 5, shown in part. The inputs are $l=180.0^\circ$, $b=0.0^\circ$, $r=0.1^\circ$, and $d=3.3$ kpc, and the fit returns $E(B - V) = 0.92$ mag.

Distance (kpc)	$E(B - V)$ (mag)
0.00	0.00
0.20	0.15
0.40	0.15
0.60	0.20
...	...
2.62	0.92
2.82	0.92
3.02	0.92
3.22	0.92
3.42	0.92
3.62	0.92
...	...

of data. Specifically, when the queried extinction data number fewer than 30, the program reports that the data are too few to fit and instead gives a median line computed from the queried extinction data; when the number is between 30 and 120, the program divides the data into two to six intervals according to the data amount and invokes MCMC to fit the distance–extinction curve; and when the number exceeds 120, the program divides the line of sight into intervals of 0.2 kpc each by distance and invokes MCMC to fit the distance–extinction curve. In addition, when the distance entered by the user exceeds the maximum distance of the queried data, the program reports that the input distance is too large for the model to give a reliable $E(B - V)$ and asks for a smaller distance; in this case the program still invokes MCMC to fit the distance–extinction curve but does not return the $E(B - V)$ at the input distance. The program finally provides $E(BP - RP)$ and A_V , which by default are converted using the extinction coefficients of Chen et al. (2019), namely $E(BP - RP) = E(B - V) \times 1.33$ and $A_V = E(B - V) \times 3.1$, while users may also choose other extinction laws to convert to the extinction in any band according to their scientific needs.

Fig. 4 shows the query result of the GSED website in Galactic coordinates. The top of the figure lists the input Galactic coordinates $l=180.0^\circ$ and $b=0.0^\circ$, the search radius $r=0.1^\circ$, the distance $d=3.3$ kpc, and the fitted $E(B - V)=0.92$ mag. The red curve is the extinction curve obtained by fitting the data, which increases gradually with distance. In general, the distance–extinction fit agrees well with the variation of the individual stellar extinction with distance and reflects the extinction variation of this region well. The text below

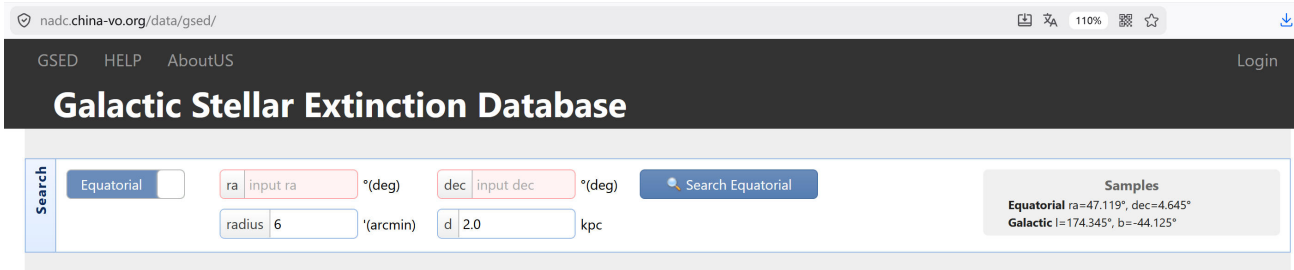


Figure 3. Query interface of the GSED website in equatorial-coordinate mode. Users can enter the right ascension (RA) and declination (Dec) and may also switch to Galactic coordinates, and example coordinates are provided on the right of the interface.

Table 5. Extinction catalogue obtained for the Galactic coordinate $l=180.0^\circ$, $b=0.0^\circ$ with a search radius $r=0.1^\circ$, showing the eight random rows.

RA (deg)	Dec (deg)	l (deg)	b (deg)	d (kpc)	d_{err} (kpc)	e (mag)	e_{err} (mag)	Source
86.325358	28.915015	179.981725	-0.070508	1.26	0.14	0.15	0.13	Green19
86.32879	28.914285	179.983915	-0.068326	3.11	1.66	0.72	0.14	Green19
86.401051	28.935686	179.998624	-0.003197	5.48	1.57	1.04	0.15	Green19
86.405988	28.948444	179.989986	0.007138	0.70	0.07	0.14	0.02	Chen19
86.406765	28.935344	180.001521	0.000893	3.43	1.58	0.87	0.13	Green19
86.419334	29.016804	179.937718	0.052713	1.01	0.05	0.27	0.02	Zhang25
86.437749	28.938147	180.013254	0.025499	0.77	0.01	0.22	0.06	Chen19
86.438797	29.017956	179.945599	0.067845	2.89	0.41	0.91	0.02	Zhang25

the figure describes the conversion based on the extinction coefficients of Chen et al. (2019), which is used to compute the colour excess $E(BP-RP)$ in the Gaia photometric system and the extinction A_V . The bottom of the interface provides two buttons, Download Fitting Curve and Download Search Result, which export the fitted distance-extinction curve data as shown in Table 4 and the queried extinction catalogue as shown in Table 5, respectively.

4.3. Limitations and Future Work

At present the query function of GSED is oriented mainly toward a single line of sight, where the user enters one coordinate, search radius, and target distance each time and the system returns the extinction curve and extinction value along that direction. This design suits the extinction correction of individual objects or specific lines of sight but cannot efficiently handle the bulk extinction queries needed, for example, correcting extinction for a large stellar sample distributed across diverse sightlines, or generating extinction maps over multiple regions. The main difficulty of bulk queries is that the query for each line of sight requires a real-time database retrieval and an MCMC fit of the distance-extinction curve, so the computational cost grows linearly with the number of queries, while the stellar sam-

ple density and extinction morphology differ markedly among lines of sight and are difficult to accelerate with a unified parameterisation.

We plan to provide a bulk-query entry in future versions, reducing the latency of large-scale queries through parallel computing and caching strategies and exploring a precomputed step-model parameterisation to replace the real-time MCMC fit, thereby balancing accuracy and efficiency. Future directions also include continuously incorporating newly released extinction catalogues to extend the coverage and distance depth of GSED, using richer stellar parameters such as the extinction curve $R(V)$ to provide wavelength-dependent extinction information, and developing a Python package so that users can call the query and fitting functions of GSED directly in their local programs.

5. SUMMARY

We construct the GSED and normalise six representative 3D extinction datasets onto a common baseline of the colour excess $E(B-V)$ and parallax distance. To place the six datasets onto a common system, we design a six-layer MLP framework with two identical branches: one for extinction, which takes the raw extinction together with the available stellar parameters or intrinsic colours of each catalogue as input and is supervised

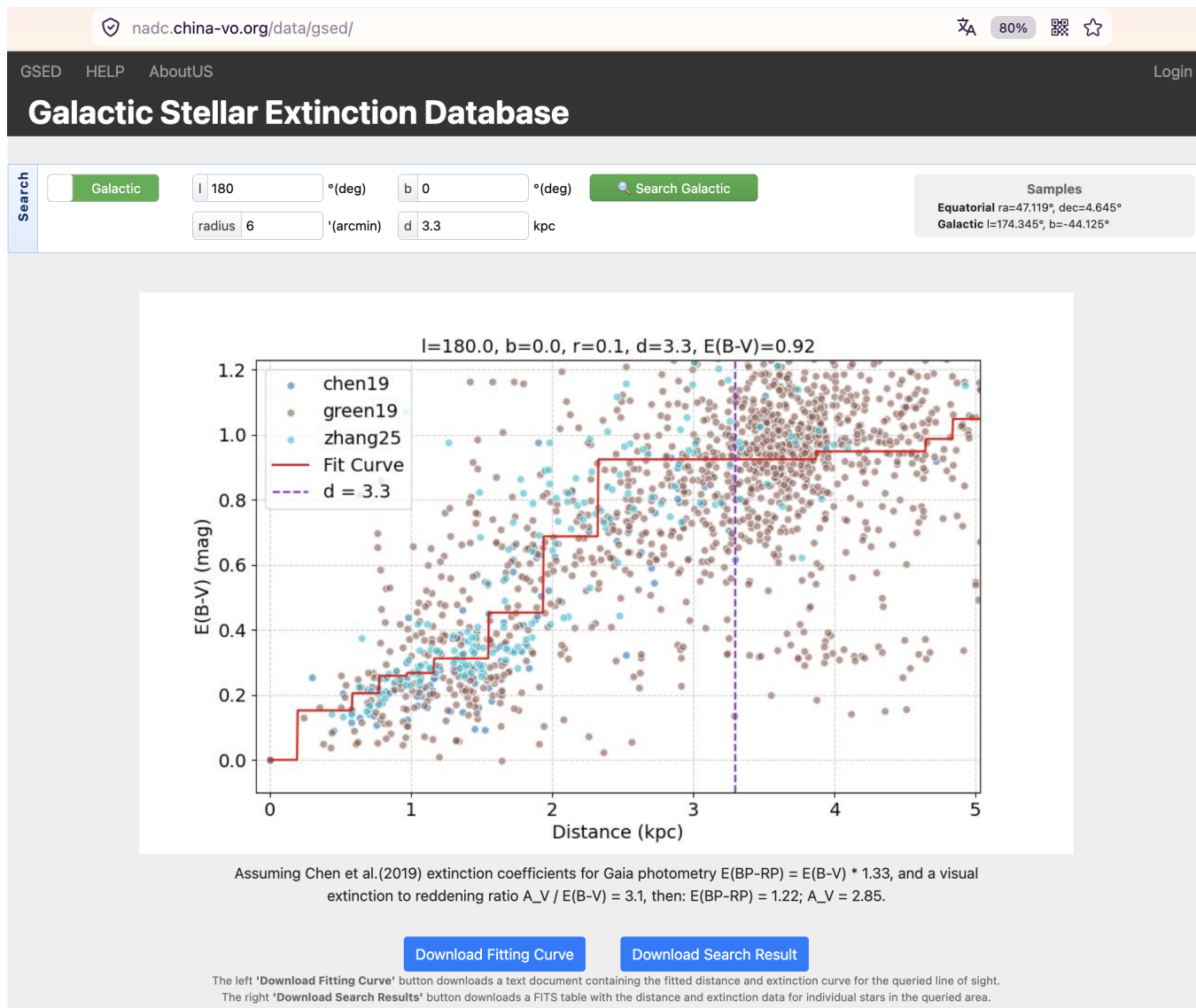


Figure 4. Query result of the GSED website in Galactic coordinates. After a user enters the Galactic longitude $l=180.0^\circ$, the Galactic latitude $b=0.0^\circ$, the search radius $r=6'$, and the target distance $d=3.3$ kpc, the system returns the extinction–distance relation of the stars along this line of sight. The coloured scatter points represent the queried stellar sample, with different colours corresponding to extinction data from different sources, namely Chen19, Green19, and Zhang25; the red step-like curve is the extinction–distance relation obtained by fitting the data; and the purple vertical dashed line marks the target distance $d=3.3$ kpc entered by the user.

by the $E(B - V)$ of Wang et al. (2025), and one for distance, which takes the Galactic coordinates and the raw distance as input and is supervised by the parallax-based distances of Zhang25. Both branches effectively learn and remove the systematic differences inherent in the heterogeneous input catalogues. The colour excesses and distances produced by the model show no apparent systematic difference relative to the supervision values, indicating that the framework learns the complex mappings among heterogeneous datasets effectively. Applying the trained models to the raw data, we obtain a homogenised stellar extinction catalogue of 1,935,987,083

entries in total and use it to draw an all-sky 3D extinction map of the Galaxy. Unlike traditional extinction maps that output only voxelised extinction values, GSED uses raw stellar data as its storage unit, supports a user-defined query radius, automatically invokes an MCMC fit of the distance–extinction curve, and provides $E(B - V)$, $E(G_{BP} - G_{RP})$, and A_V directly.

The core advantage of GSED lies in its extensibility, as the systematic-correction and distance-correction framework established here can be reused for future extinction datasets without rebuilding from scratch. At the functional level, the current query is oriented mainly toward

a single line of sight, and in the future we will provide a bulk-query interface that reduces the computational cost of large-scale extinction correction through parallel computing and pre-fitting strategies, together with a Python package that supports local use. At the data level, as new-generation surveys such as Gaia DR4, CSST, and LSST advance, higher-precision parallaxes and deeper multi-band photometry will further improve the quality of extinction measurements and distance estimates, and the data volume, coverage depth, and parameter richness of GSED will grow accordingly. More accurate extinction data not only help to improve the resolution and reliability of the 3D dust structure of the Galaxy, but also provide a data basis for finer studies of the interstellar medium, such as the spatial variation

of the dust extinction curve and the internal extinction law of molecular clouds. We expect GSED to become a common infrastructure for extinction correction in the Galaxy and to evolve continuously as observational data and functionality grow richer.

- 1 This work is supported by the National Key Research
- 2 and Development Program of China 2024YFA1611601,
- 3 the National Natural Science Foundation of China
- 4 12322304, National Natural Science Foundation of Yun-
- 5 nan Province 202301AV070002, and the Xingdian talent
- 6 support programme of Yunnan Province. We acknowl-
- 7 edge the science research grants from the China Manned
- 8 Space Project with no. CMS-CSST-2025-A11.

REFERENCES

- Amôres, E. B., Jesus, R. M., Moitinho, A., et al. 2021, *MNRAS*, 508, 1788, doi: 10.1093/mnras/stab2248
- Berry, M., Ivezić, Ž., Sesar, B., et al. 2012, *ApJ*, 757, 166, doi: 10.1088/0004-637X/757/2/166
- Chambers, K. C., Magnier, E. A., Metcalfe, N., et al. 2016, arXiv e-prints, arXiv:1612.05560, doi: 10.48550/arXiv.1612.05560
- Chen, B.-Q., Liu, X.-W., Yuan, H.-B., Huang, Y., & Xiang, M.-S. 2015, *MNRAS*, 448, 2187, doi: 10.1093/mnras/stv103
- Chen, B. Q., Schultheis, M., Jiang, B. W., et al. 2013, *A&A*, 550, A42, doi: 10.1051/0004-6361/201219682
- Chen, B.-Q., Liu, X.-W., Yuan, H.-B., et al. 2014, *MNRAS*, 443, 1192, doi: 10.1093/mnras/stu1192
- Chen, B.-Q., Huang, Y., Yuan, H.-B., et al. 2019, *MNRAS*, 483, 4277, doi: 10.1093/mnras/sty3341
- Draine, B. T. 2003, *ARA&A*, 41, 241, doi: 10.1146/annurev.astro.41.011802.094840
- Edenhofer, G., Zucker, C., Frank, P., et al. 2024, *A&A*, 685, A82, doi: 10.1051/0004-6361/202347628
- Gaia Collaboration, Brown, A. G. A., Vallenari, A., et al. 2018, *A&A*, 616, A1, doi: 10.1051/0004-6361/201833051
- Gaia Collaboration, Vallenari, A., Brown, A. G. A., et al. 2023, *A&A*, 674, A1, doi: 10.1051/0004-6361/202243940
- Gontcharov, G. A., Marchuk, A. A., Savchenko, S. S., et al. 2025, *Research in Astronomy and Astrophysics*, 25, 125016, doi: 10.1088/1674-4527/ae12a6
- Gonzalez, O. A., Rejkuba, M., Zoccali, M., et al. 2012, *A&A*, 543, A13, doi: 10.1051/0004-6361/201219222
- Green, G. 2018, *The Journal of Open Source Software*, 3, 695, doi: 10.21105/joss.00695
- Green, G. M., Schlafly, E., Zucker, C., Speagle, J. S., & Finkbeiner, D. 2019, *ApJ*, 887, 93, doi: 10.3847/1538-4357/ab5362
- Green, G. M., Schlafly, E. F., Finkbeiner, D. P., et al. 2015, *ApJ*, 810, 25, doi: 10.1088/0004-637X/810/1/25
- Green, G. M., Schlafly, E. F., Finkbeiner, D., et al. 2018, *MNRAS*, 478, 651, doi: 10.1093/mnras/sty1008
- Guo, H.-L., Chen, B.-Q., Yuan, H.-B., et al. 2021, *ApJ*, 906, 47, doi: 10.3847/1538-4357/abc68a
- Hanson, R. J., Bailer-Jones, C. A. L., Burgett, W. S., et al. 2016, *MNRAS*, 463, 3604, doi: 10.1093/mnras/stw2240
- Lindgren, L., Bastian, U., Biermann, M., et al. 2021, *A&A*, 649, A4, doi: 10.1051/0004-6361/202039653
- Marshall, D. J., Robin, A. C., Reylé, C., Schultheis, M., & Picaud, S. 2006, *A&A*, 453, 635, doi: 10.1051/0004-6361:20053842
- Planck Collaboration, Abergel, A., Ade, P. A. R., et al. 2014, *A&A*, 571, A11, doi: 10.1051/0004-6361/201323195
- Saydjari, A. K., Schlafly, E. F., Lang, D., et al. 2023, *ApJS*, 264, 28, doi: 10.3847/1538-4365/aca594
- Schlegel, D. J., Finkbeiner, D. P., & Davis, M. 1998, *ApJ*, 500, 525, doi: 10.1086/305772
- Schultheis, M., Ganesh, S., Simon, G., et al. 1999, *A&A*, 349, L69, doi: 10.48550/arXiv.astro-ph/9908349
- Schultheis, M., Chen, B. Q., Jiang, B. W., et al. 2014, *A&A*, 566, A120, doi: 10.1051/0004-6361/201322788
- Shen, H., Chen, B.-Q., Guo, H.-L., et al. 2022, *MNRAS*, 514, 4398, doi: 10.1093/mnras/stac1615
- Skrutskie, M. F., Cutri, R. M., Stiening, R., et al. 2006, *AJ*, 131, 1163, doi: 10.1086/498708
- Sun, M., Chen, B., Guo, H., et al. 2023, *AJ*, 166, 126, doi: 10.3847/1538-3881/ace5ab

- Sun, M., Chen, B., Sun, B., et al. 2025, *Research in Astronomy and Astrophysics*, 25, 057002, doi: 10.1088/1674-4527/adc5e1
- Trumpler, R. J. 1930, *PASP*, 42, 214, doi: 10.1086/124039
- Wang, T., Yuan, H., Chen, B., et al. 2025, *ApJS*, 280, 15, doi: 10.3847/1538-4365/adea39
- Wolf, C., Onken, C. A., Luvaul, L. C., et al. 2018, *PASA*, 35, e010, doi: 10.1017/pasa.2018.5
- Yu, J., Casagrande, L., Taylor, J. A., et al. 2026, *MNRAS*, 549, stag848, doi: 10.1093/mnras/stag848
- Yuan, H. B., Liu, X. W., & Xiang, M. S. 2013, *MNRAS*, 430, 2188, doi: 10.1093/mnras/stt039
- Zhang, R., & Yuan, H. 2023, *ApJS*, 264, 14, doi: 10.3847/1538-4365/ac9dfa
- Zhang, X., & Green, G. M. 2025, *Science*, 387, 1209, doi: 10.1126/science.ado9787
- Zhang, X., Green, G. M., & Rix, H.-W. 2023, *MNRAS*, 524, 1855, doi: 10.1093/mnras/stad1941
- Zhao, G., Zhao, Y.-H., Chu, Y.-Q., Jing, Y.-P., & Deng, L.-C. 2012, *Research in Astronomy and Astrophysics*, 12, 723, doi: 10.1088/1674-4527/12/7/002
- Zucker, C., Saydjari, A. K., Speagle, J. S., et al. 2025, *ApJ*, 992, 39, doi: 10.3847/1538-4357/adfbef6

APPENDIX

A. PER-CATALOGUE RESULTS OF THE EXTINCTION-SYSTEMATICS CORRECTION

A.1. *Green19*

Cross-matching the Green19 extinction data, which include the intrinsic colour $(g-r)_0$, with the Wang et al. (2025) catalogue, and applying an `[Fe/H]` error limit of `feh_err<0.3` together with a non-negative extinction selection, yields 2,055,902 common entries, which we split randomly into training and test sets in a ratio of 8:2. Fig. 5 compares the extinction residuals before and after the correction as a function of E_{Green19} . After the MLP correction, the median residual stays near zero and shows no systematic drift as E_{Green19} increases, indicating that the model prediction $E(B-V)_{\text{model}}$ is stable. In contrast, the raw E_{Green19} carries a marked extinction-dependent systematic difference relative to the baseline $E(B-V)_{\text{Wang25}}$, with an acceptable residual when $E_{\text{Green19}} < 0.8$ mag but a residual exceeding 1 mag in the high-extinction regime where $E_{\text{Green19}} > 1.5$ mag, which reflects a severe underestimate. Fig. 6 compares the residuals as a function of $(g-r)_0$. The MLP-corrected value agrees closely with the baseline across the full range of $(g-r)_0$, whereas the raw Green19 extinction is systematically low at the blue end where $(g-r)_0 < 0.1$. Fig. 7 compares the residuals as a function of `[Fe/H]`. After the correction the residual shows no clear trend within `[Fe/H] ∈ [-0.5, 0.5]`, while the raw data are slightly high at the metal-poor end, and the model corrects this bias effectively. For a few stars without $(g-r)_0$ information, we use the samples that have colour information to establish a linear relation between $E(B-V)_{\text{model}}$ and E_{Green19} , applying 3σ clipping to remove outliers and repeating five times, and the best-fit line is $Y = 0.93X + 0.0087$, with which the systematic correction is completed.

A.2. *Chen19*

Cross-matching the Chen19 extinction data with the Wang et al. (2025) extinction catalogue yields 815,573 records. We impose the constraints `E(BP-RP)_Chen19 >= 0` and `E(B-V)_Wang25 >= 0` on the matched data, and after this processing 810,808 common entries remain, which we split randomly into training and test sets in a ratio of 8:2. Fig. 8 compares the residuals as a function of $E(BP-RP)_{\text{Chen19}}$. After the MLP correction the median residual lies close to the zero line, whereas the raw $E(BP-RP)_{\text{Chen19}}$ still deviates slightly from the baseline after conversion with the extinction coefficient, and the model corrects this bias effectively. Fig. 9 compares the residuals as a function of $(BP-RP)_0$. The MLP-corrected residuals remain consistent across spectral types, whereas the raw data deviate nonlinearly as the colour reddens, and the model removes this trend effectively.

A.3. *Guo21*

Cross-matching the Guo21 extinction data with the Wang et al. (2025) extinction catalogue yields 127,861 records. We impose the constraints `A_r_Guo21 >= 0` and `E(B-V)_Wang25 >= 0` on the matched data, and after this processing 124,147 common entries remain. Fig. 10 compares the residuals as a function of $A_{r,\text{Guo21}}$. The MLP-corrected residuals lie close to the zero line across the full range of extinction, whereas the raw $A_{r,\text{Guo21}}$ shows a systematic negative offset as the extinction increases, which the model corrects effectively. Fig. 11 compares the residuals as a function of $(BP-RP)_0$. After the correction the residuals of stars of different spectral types are well consistent, and both the scatter and the systematic offset of the raw data are improved.

A.4. *Sun25*

Cross-matching the Sun25 extinction data with the Wang et al. (2025) extinction catalogue yields 338,683 records. We impose the constraints `Teff_err < 500`, `feh_err < 0.3`, `E(BP-RP)_Sun25 >= 0`, and `E(B-V)_Wang25 >= 0` on the matched data, where `Teff_err` is the error of the effective temperature T_{eff} in the Sun25 catalogue and `feh_err` is the error of `[Fe/H]` in the Sun25 catalogue. After this processing 124,147 common entries remain. Fig. 12 compares the residuals as a function of $E(BP-RP)$. The MLP-corrected median residual lies essentially on the zero line, whereas the raw Sun25 extinction shows a slight systematic negative offset in the low-extinction regime. Fig. 13 compares the residuals as a function of T_{eff} . After the correction the residuals are evenly distributed within the range of 4000 to 8000 K, whereas the raw data have a large scatter at the high-temperature end, which the model compresses effectively. Fig. 14 compares the residuals as a function of `[Fe/H]`. After the MLP correction the residuals concentrate around zero, whereas the raw data carry a slight positive offset, which the model removes effectively.

A.5. *Zhang25*

Cross-matching the Zhang25 extinction data with the Wang et al. (2025) extinction catalogue yields 4,677,295 records. We impose the constraints `quality_flags < 8`, `feh_confidence > 0.5`, `logg_confidence > 0.5`, `teff_confidence > 0.5`, `Teff_err < 0.5`, `feh_err < 0.3`, `logg_err < 0.3`, `E_Zhang25 >= 0`, and `E(B-V)_Wang25 >= 0` on the matched data, where `quality_flags` represents the quality of the stellar parameters in the Zhang25 catalogue, `feh_confidence`, `logg_confidence`, and `teff_confidence` are the confidence estimates of the effective temperature T_{eff} , the metallicity [Fe/H], and the surface gravity $\log g$ in the Zhang25 catalogue, and `Teff_err`, `feh_err`, and `logg_err` are the errors of the effective temperature T_{eff} in kilokelvin (kK), the metallicity [Fe/H], and the surface gravity $\log g$ in the Zhang25 catalogue. After this processing 3,792,623 common entries remain. Fig. 15 compares the residuals as a function of E_{Zhang25} . The extinction of the Zhang25 catalogue is already close to the baseline, so the magnitude of the correction is smaller than for the other catalogues, yet the MLP still compresses the residual scatter further. Fig. 16 compares the residuals as a function of T_{eff} . After the MLP correction the residuals fluctuate little, whereas the raw data have a relatively large scatter, and the model improves the consistency of the extinction effectively. Fig. 17 compares the residuals as a function of [Fe/H]. After the MLP correction the residuals stay near zero, whereas the raw residuals are slightly below zero, and the model removes this bias effectively.

A.6. *Zucker25*

Since the Zucker25 catalogue and the Wang et al. (2025) extinction catalogue do not overlap, we cross-match the Zucker25 catalogue with the Zhang25 catalogue, which yields 65,307,607 records. We impose the constraints `Teff_err < 0.5`, `feh_err < 0.3`, `logg_err < 0.3`, `A_V_Zucker25 >= 0`, and `E(B-V)_Zhang25_model >= 0` on the matched data, where `Teff_err`, `feh_err`, and `logg_err` are the errors of the effective temperature T_{eff} , the metallicity [Fe/H], and the surface gravity $\log g$ in the Zucker25 catalogue, and `E(B-V)_Zhang25_model` is the colour excess obtained from the model in the Zhang25 catalogue. After this processing 47,862,741 common entries remain. Fig. 18 compares the residuals as a function of $A_{V_Zucker25}$. The MLP-corrected median residual lies close to the zero line, whereas the raw $A_{V_Zucker25}$ shows a marked systematic positive offset relative to the baseline after conversion with a fixed extinction coefficient, which is especially prominent in the high-extinction regime. Fig. 19 compares the residuals as a function of T_{eff} . After the correction the residuals show no clear trend across the full range of T_{eff} , and both the systematic bias and the scatter of the raw data are suppressed effectively. Fig. 20 compares the residuals as a function of [Fe/H]. After the MLP correction the residuals concentrate around zero, whereas the raw residuals are markedly positive and fluctuate considerably, and the model removes this bias effectively.

B. PER-CATALOGUE RESULTS OF THE DISTANCE-SYSTEMATICS CORRECTION

The distance baseline is taken from the Zhang25 catalogue, so for every catalogue to be calibrated we first cross-match it with Zhang25 and then select a clean baseline sample by imposing the same set of quality constraints on the Zhang25 columns, namely `quality_flags < 8`, `feh_confidence > 0.5`, `logg_confidence > 0.5`, `teff_confidence > 0.5`, `Teff_err < 0.5`, `feh_err < 0.3`, and `logg_err < 0.3`. These constraints retain only the Zhang25 stars with well-determined parameters and reliable distances, so that the baseline distance D_{Zhang25} is accurate enough to serve as the supervision value. In the following subsections we therefore report only the additional constraints imposed on each calibrated catalogue itself, without repeating the Zhang25 baseline selection. In every case, the figures compare the residuals before and after the calibration as a function of the raw distance; unless noted otherwise, the MLP-calibrated median residual lies close to the zero line, with good consistency at the near end ($d < 5$ kpc) and growing scatter at the far end while the overall trend still follows the baseline, indicating that the model effectively removes the systematic bias of the raw distance.

B.1. *Green19*

Cross-matching the Green19 catalogue with the Zhang25 baseline sample yields 111,207,061 records. We further add the constraints `Mr_err < 0.5`, `feh_err < 0.3`, `d > 0`, and `d_err > 0` on the Green19 catalogue, where `Mr_err`, `feh_err`, `d`, and `d_err` are the error of the r -band absolute magnitude, the error of the metallicity [Fe/H], the distance, and the distance error in the Green19 catalogue. After this processing 36,442,106 common entries remain. As shown in Fig. 21, the raw D_{Green19} is markedly too large at the far end, and the MLP calibration removes this bias effectively.

B.2. *Chen19*

Cross-matching the Chen19 catalogue with the Zhang25 baseline sample yields 48,302,417 records, and no additional constraint is imposed on Chen19 itself. After this processing 35,122,082 common entries remain. As shown in Fig. 22, the raw D_{Chen19} is markedly too large at the far end, and the MLP calibration removes this bias effectively.

B.3. *Guo21*

Cross-matching the Guo21 catalogue with the Zhang25 baseline sample yields 16,237,365 records, and no additional constraint is imposed on Guo21 itself. After this processing 14,276,717 common entries remain. As shown in Fig. 23, the raw D_{Guo21} is markedly too large at the far end, and the MLP calibration removes this bias effectively.

B.4. *Sun25*

Cross-matching the Sun25 catalogue with the Zhang25 baseline sample yields 82,582,427 records. We further add the constraints $\text{Teff_err} < 0.5$, $\text{feh_err} < 0.3$, $\text{d} > 0$, and $\text{d_err} > 0$ on the Sun25 catalogue, where Teff_err , feh_err , d , and d_err are the error of the effective temperature T_{eff} , the error of the metallicity [Fe/H], the distance, and the distance error in the Sun25 catalogue. After this processing 60,443,839 common entries remain. As shown in Fig. 24, the raw D_{Sun25} is markedly too large at the far end, and the MLP calibration removes this bias effectively.

B.5. *Zucker25*

Cross-matching the Zucker25 catalogue with the Zhang25 baseline sample yields 65,307,607 records. We further add the constraints $\text{Teff_err} < 0.5$, $\text{feh_err} < 0.3$, $\text{logg_err} < 0.3$, $\text{d} > 0$, and $\text{d_err} > 0$ on the Zucker25 catalogue, where Teff_err , feh_err , logg_err , d , and d_err are the error of the effective temperature T_{eff} , the error of the metallicity [Fe/H], the surface gravity $\log g$, the distance, and the distance error in the Zucker25 catalogue. After this processing 27,701,929 common entries remain. As shown in Fig. 25, the raw Zucker25 distance shows the smallest systematic bias among the five catalogues, with its median residual already lying near the zero line, and after the MLP calibration the residual remains centred on zero with a slightly reduced scatter.

C. EFFECT OF METALLICITY AS AN INPUT FEATURE

Taking the Zhang25 data as an example, we test whether the input parameter [Fe/H] affects the result. When the inputs are E_{Zhang25} , T_{eff} , and [Fe/H], the best loss of the model is 0.0211, and when the inputs are E_{Zhang25} and T_{eff} , the best loss is 0.0216. Fig. 26 compares the residuals between $E(B-V)_{\text{model}}$ and the target $E(B-V)_{\text{Wang25}}$ obtained with and without [Fe/H] among the inputs, and the results of the two models are similar, with the model that includes [Fe/H] performing slightly better.

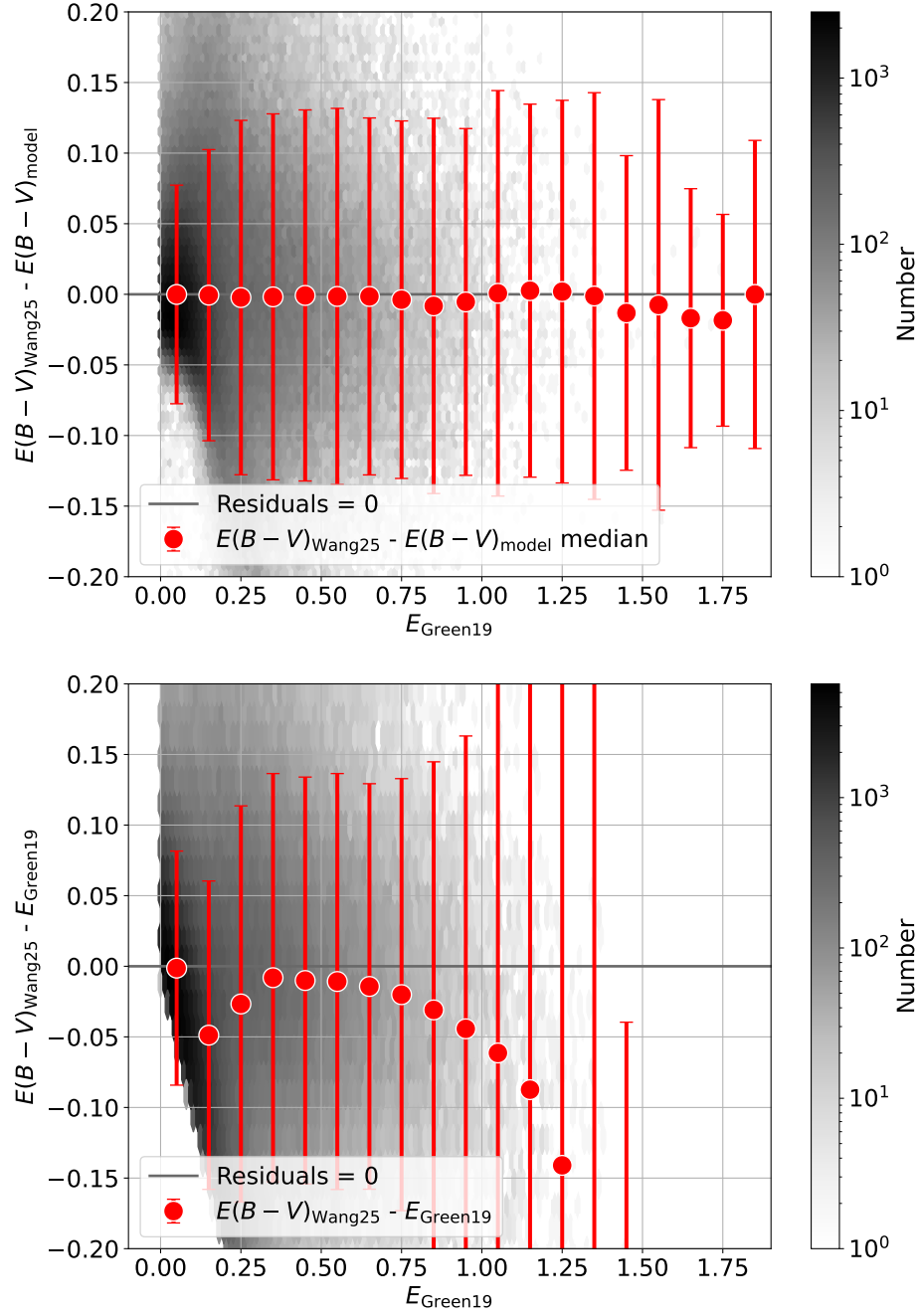


Figure 5. Median residuals shown as dots and residual density distributions of the target $E(B-V)_{Wang25}$ relative to the model prediction $E(B-V)_{model}$ in the upper panel and to $E_{Green19}$ in the bottom panel, as a function of $E_{Green19}$. The data are grouped by $E_{Green19}$ in intervals of 0.1 mag, the error bars denote the standard deviation, and the grey horizontal line marks the zero residual.

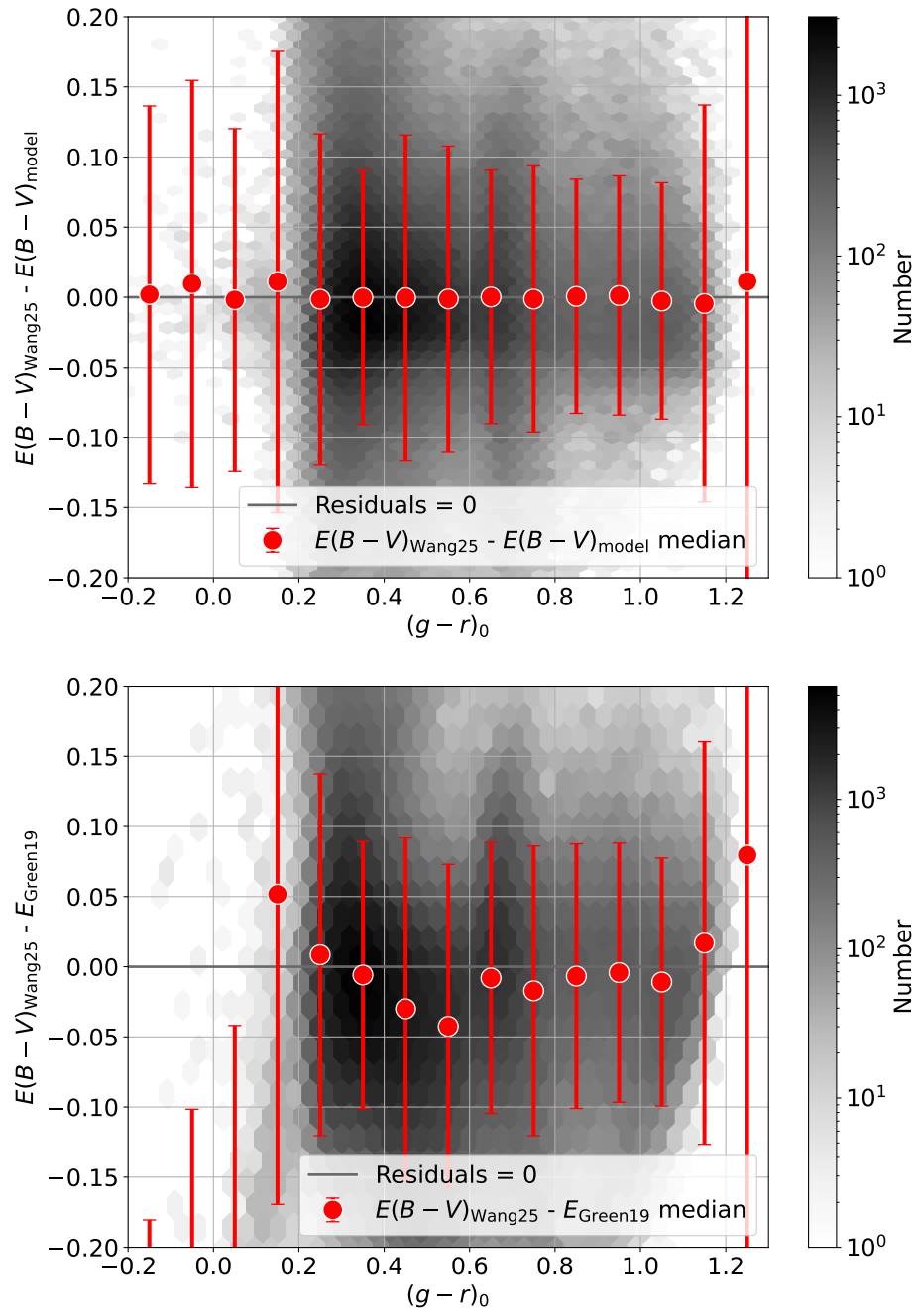


Figure 6. Same as Fig. 5, but as a function of the intrinsic colour $(g-r)_0$.

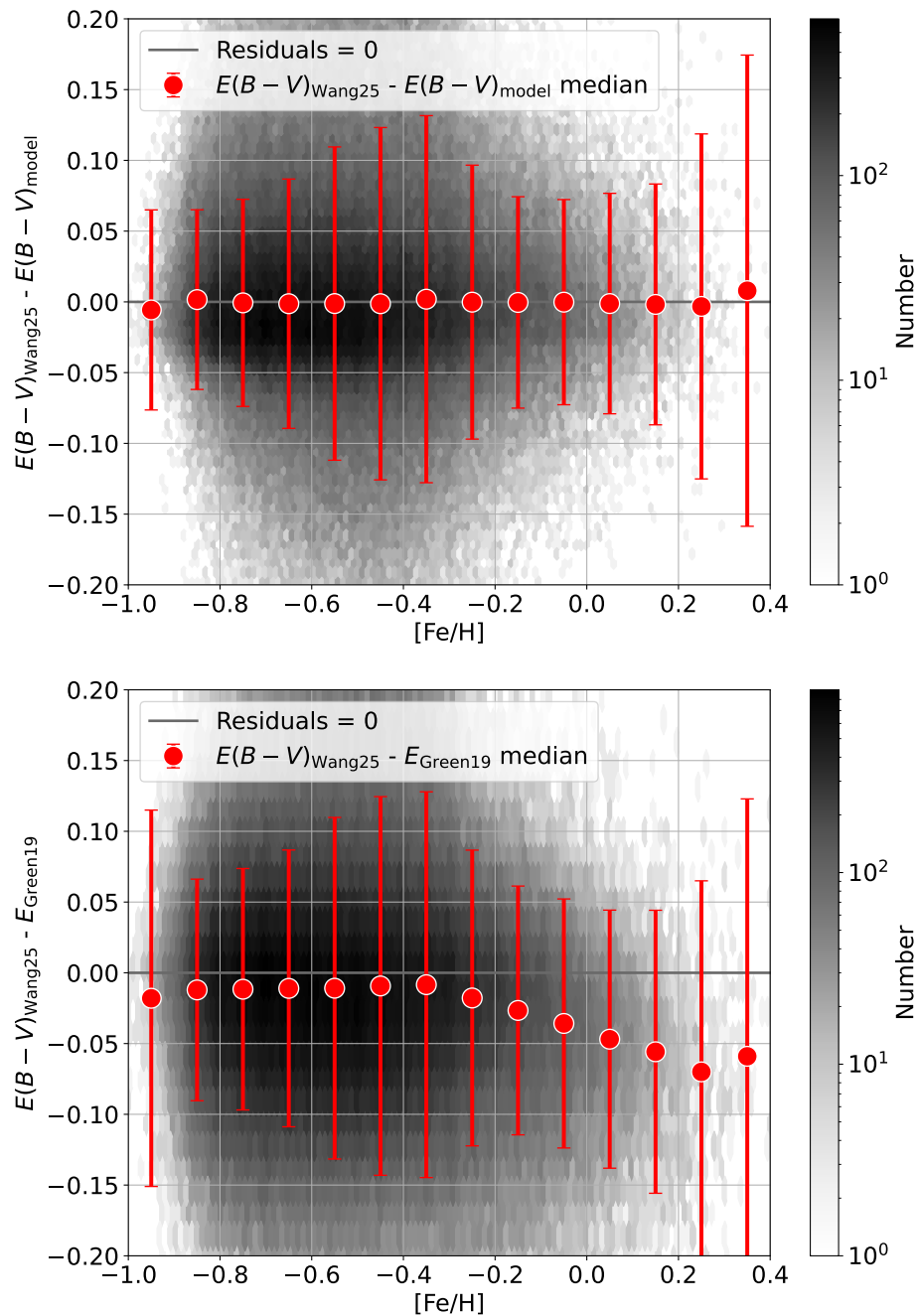


Figure 7. Same as Fig. 5, but as a function of the metallicity $[\text{Fe}/\text{H}]$.

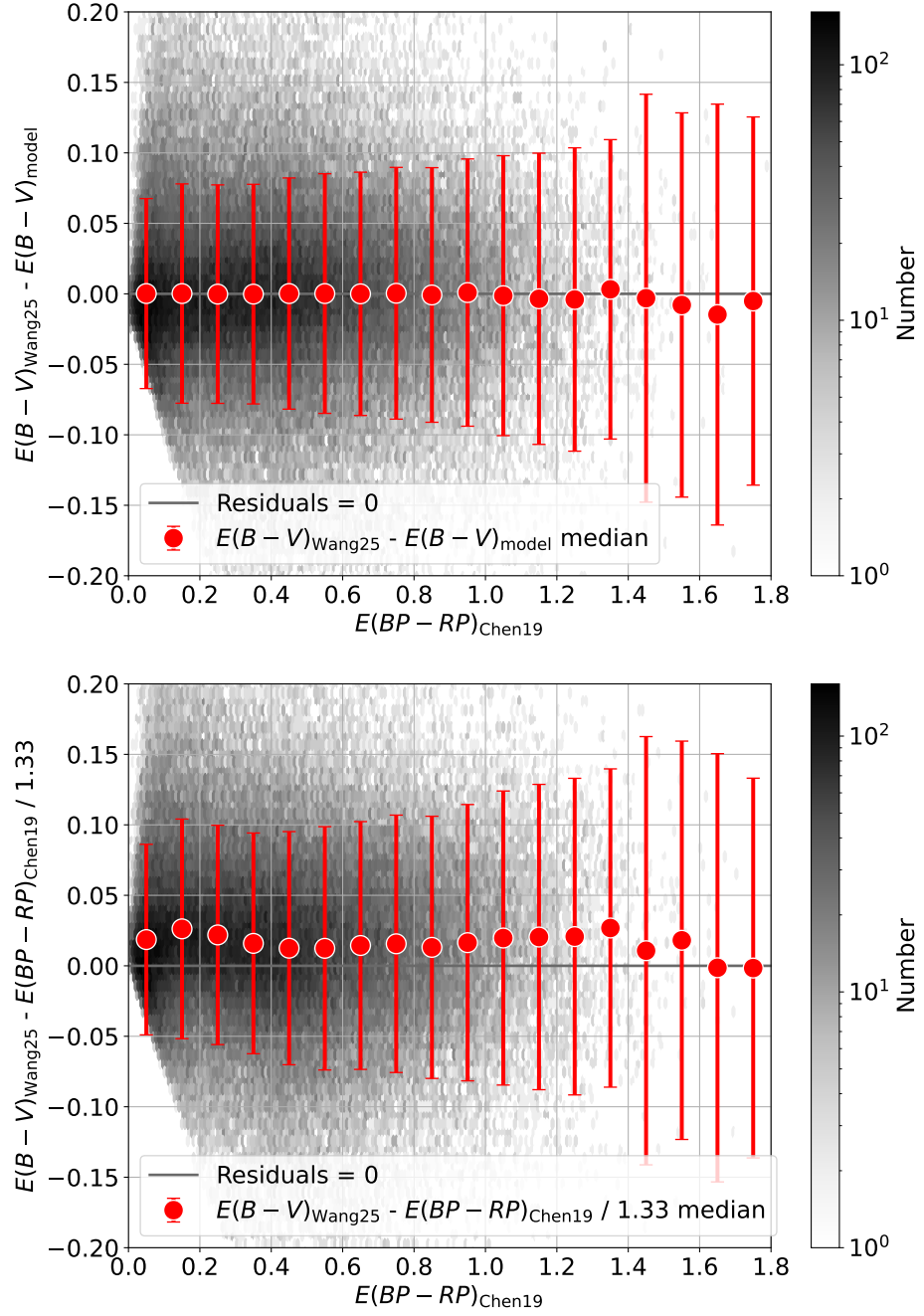


Figure 8. Median residuals and density distributions of the target $E(B-V)_{\text{Wang25}}$ relative to the model prediction $E(B-V)_{\text{model}}$ in the upper panel and to $E(BP-RP)_{\text{Chen19}}/1.33$ in the bottom panel, as a function of $E(BP-RP)_{\text{Chen19}}$.

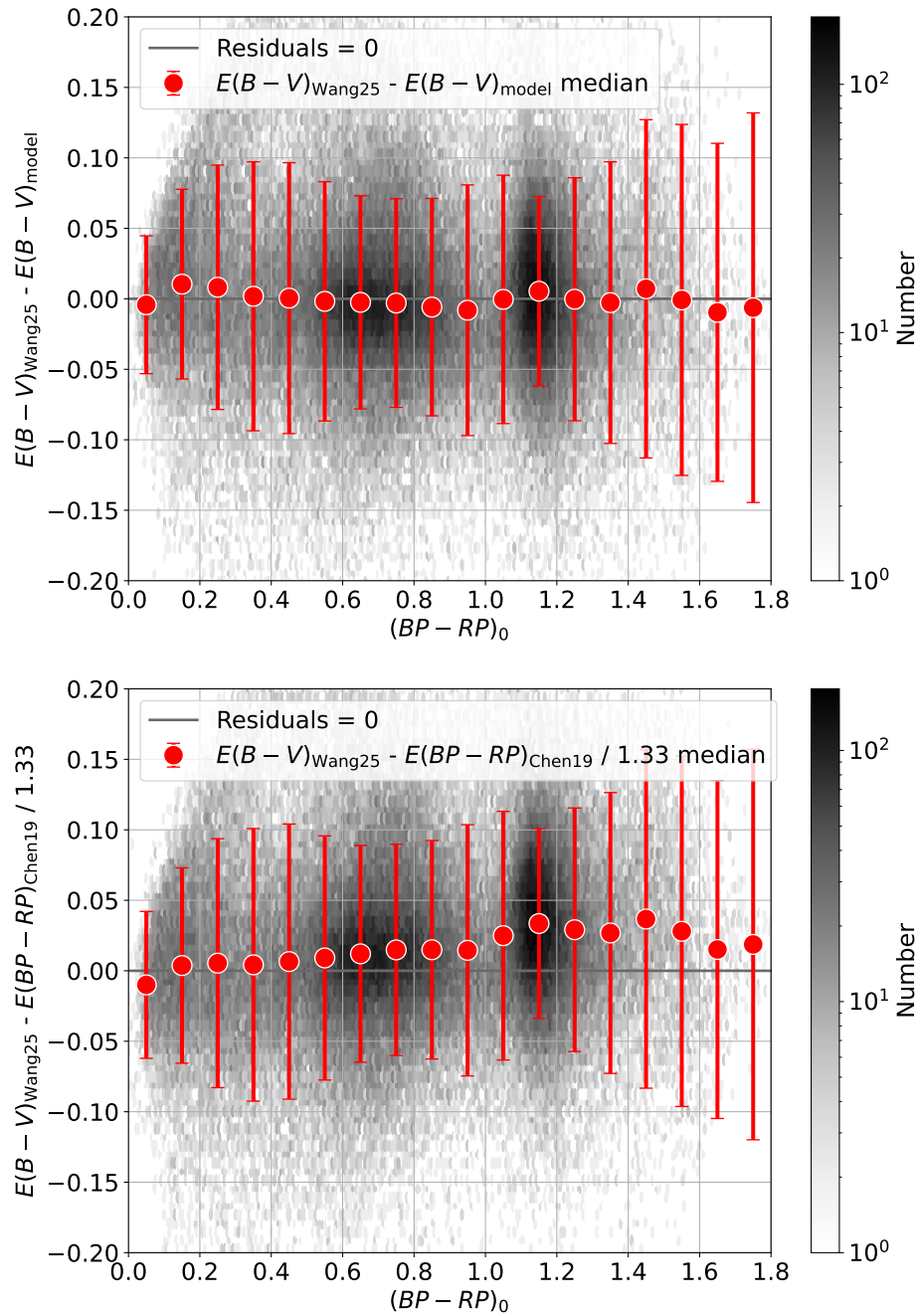


Figure 9. Same as Fig. 8, but as a function of the intrinsic colour $(BP - RP)_0$.

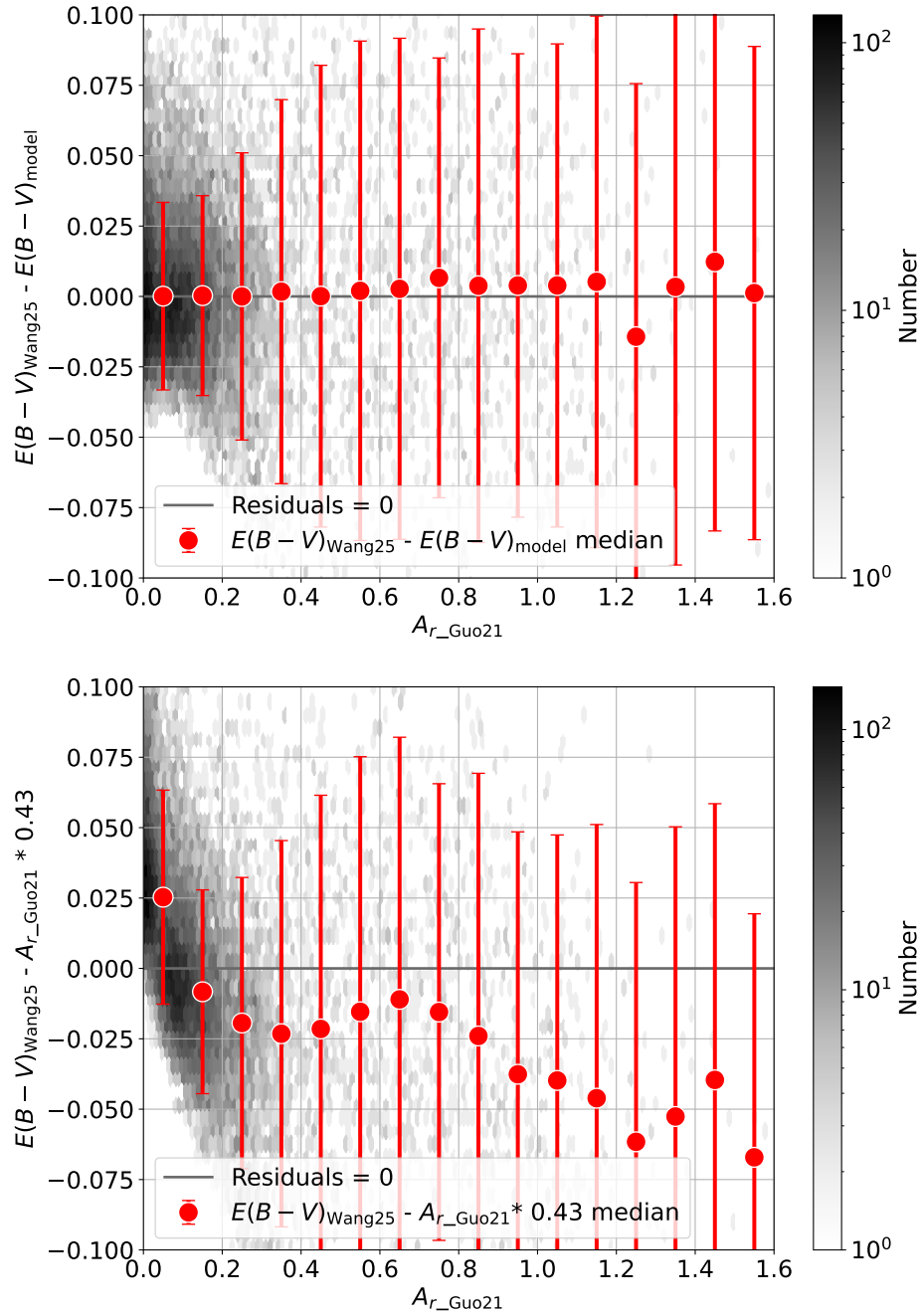


Figure 10. Median residuals and density distributions of the target $E(B-V)_{Wang25}$ relative to the model prediction $E(B-V)_{model}$ in the upper panel and to $A_{r_Guo21} \times 0.43$ in the bottom panel, as a function of A_{r_Guo21} .

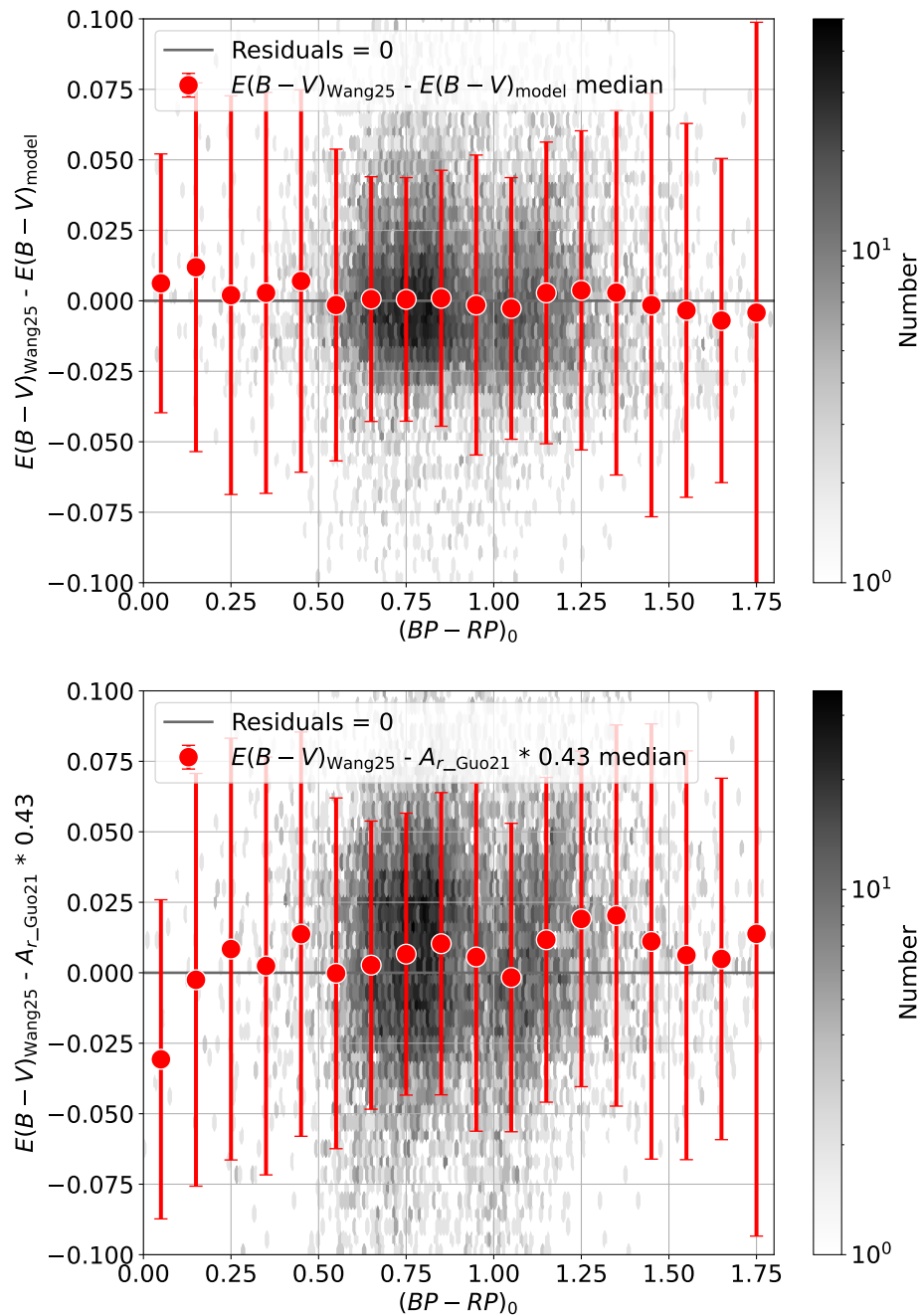


Figure 11. Same as Fig. 10, but as a function of the intrinsic colour $(BP - RP)_0$.

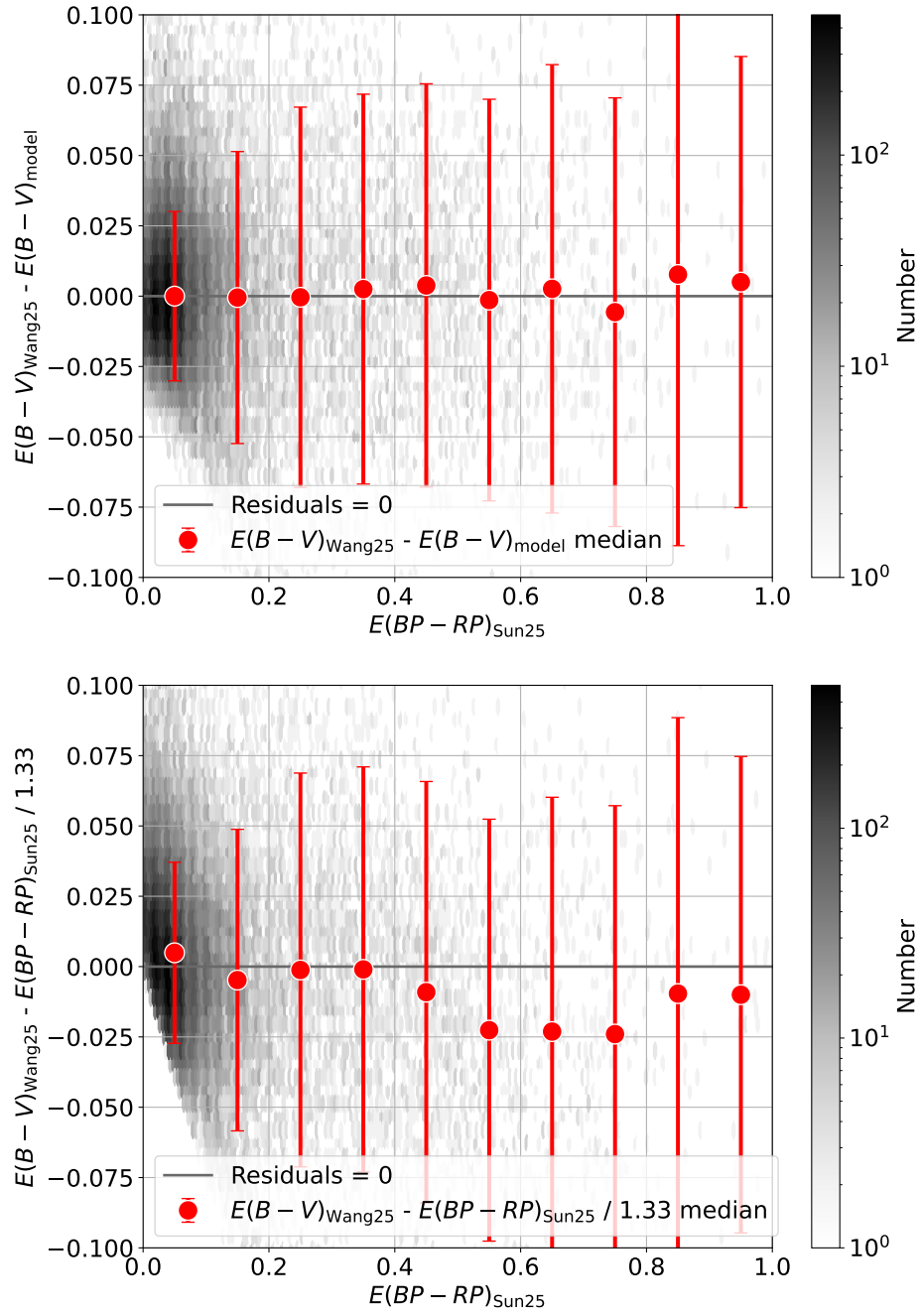


Figure 12. Median residuals and density distributions of the target $E(B - V)_{\text{Wang25}}$ relative to the model prediction $E(B - V)_{\text{model}}$ in the upper panel and to $E(BP - RP)_{\text{Sun25}}$ in the bottom panel, as a function of $E(BP - RP)_{\text{Sun25}}$.

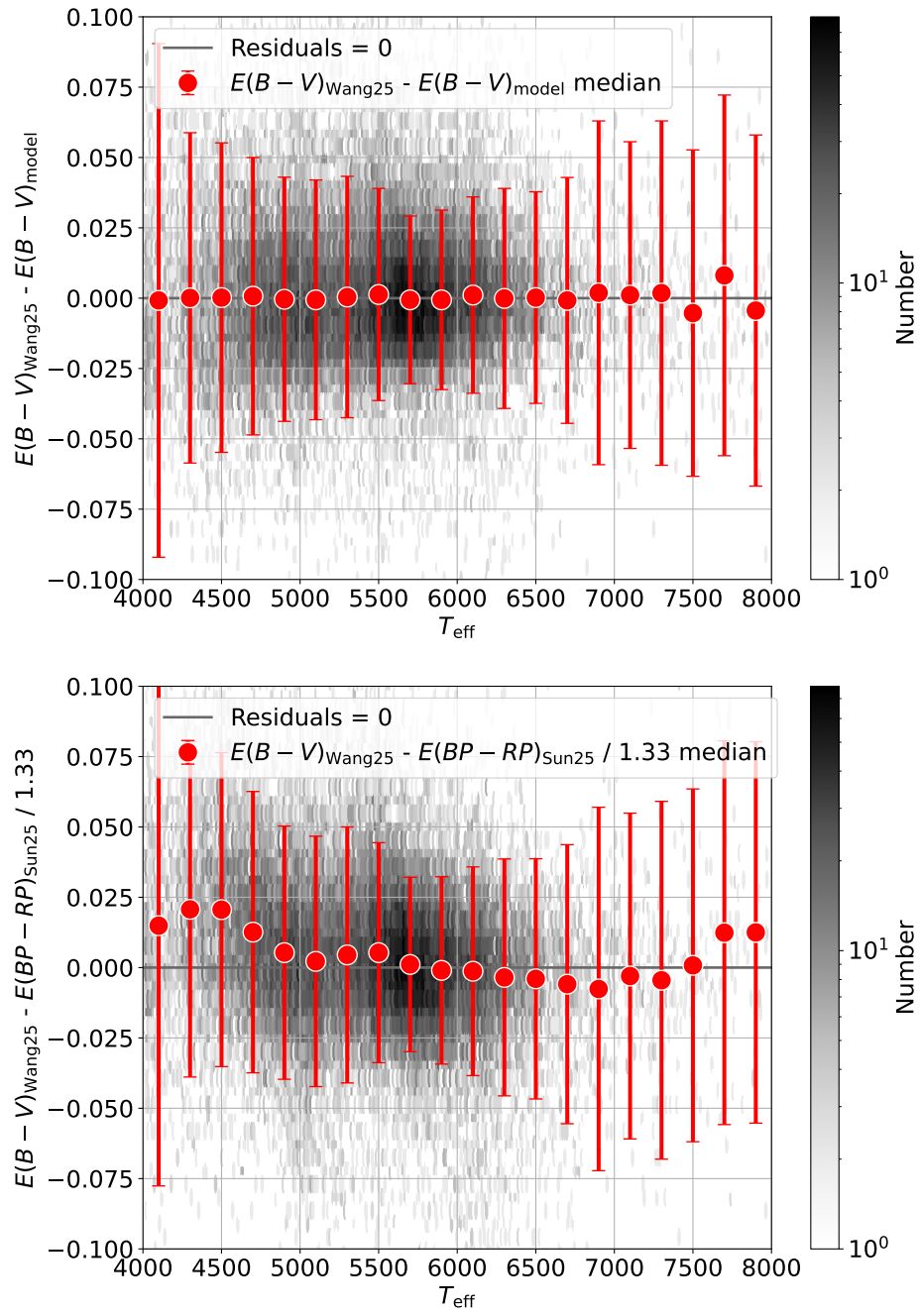


Figure 13. Same as Fig. 12, but as a function of the effective temperature T_{eff} .

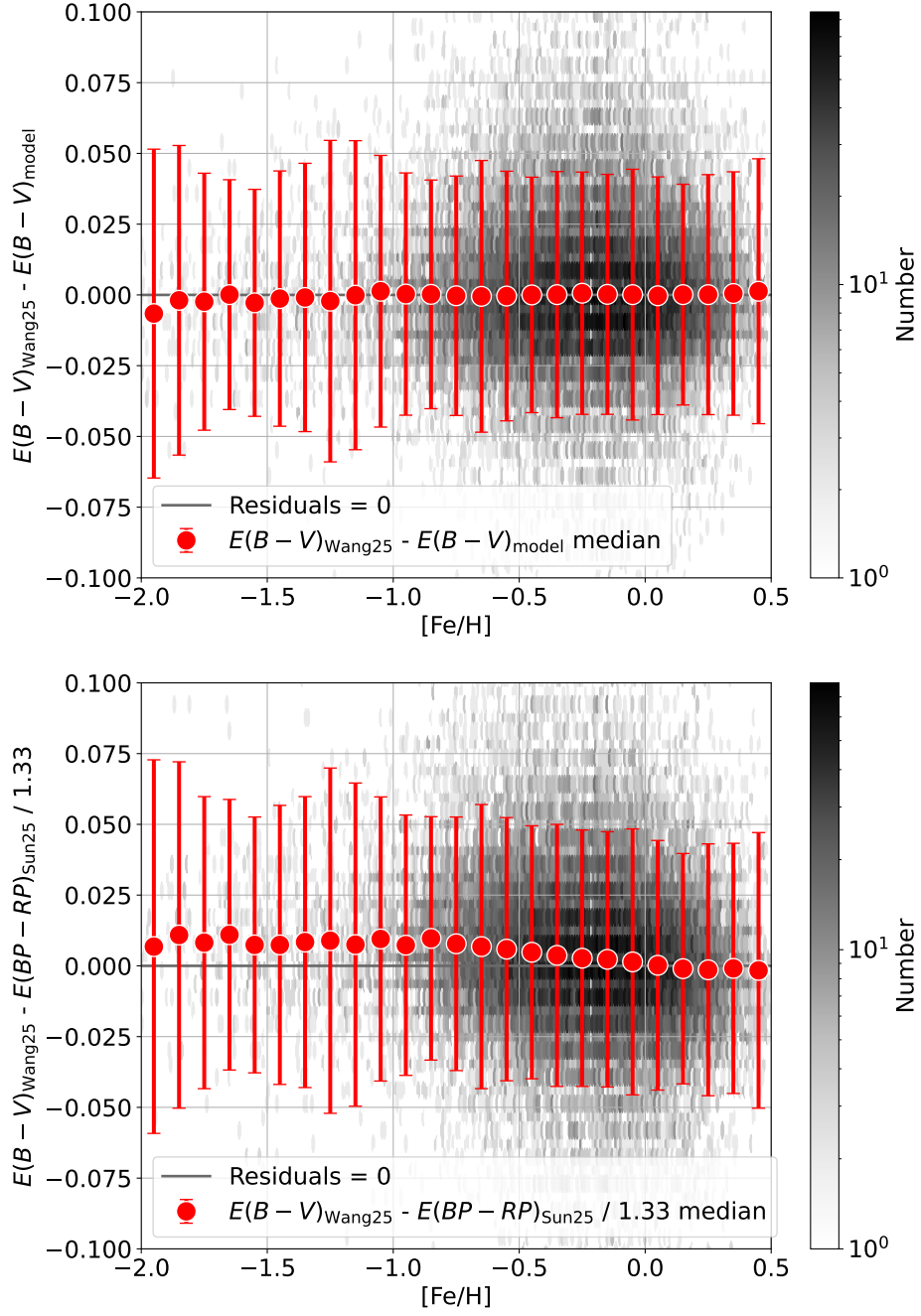


Figure 14. Same as Fig. 12, but as a function of the metallicity $[Fe/H]$.

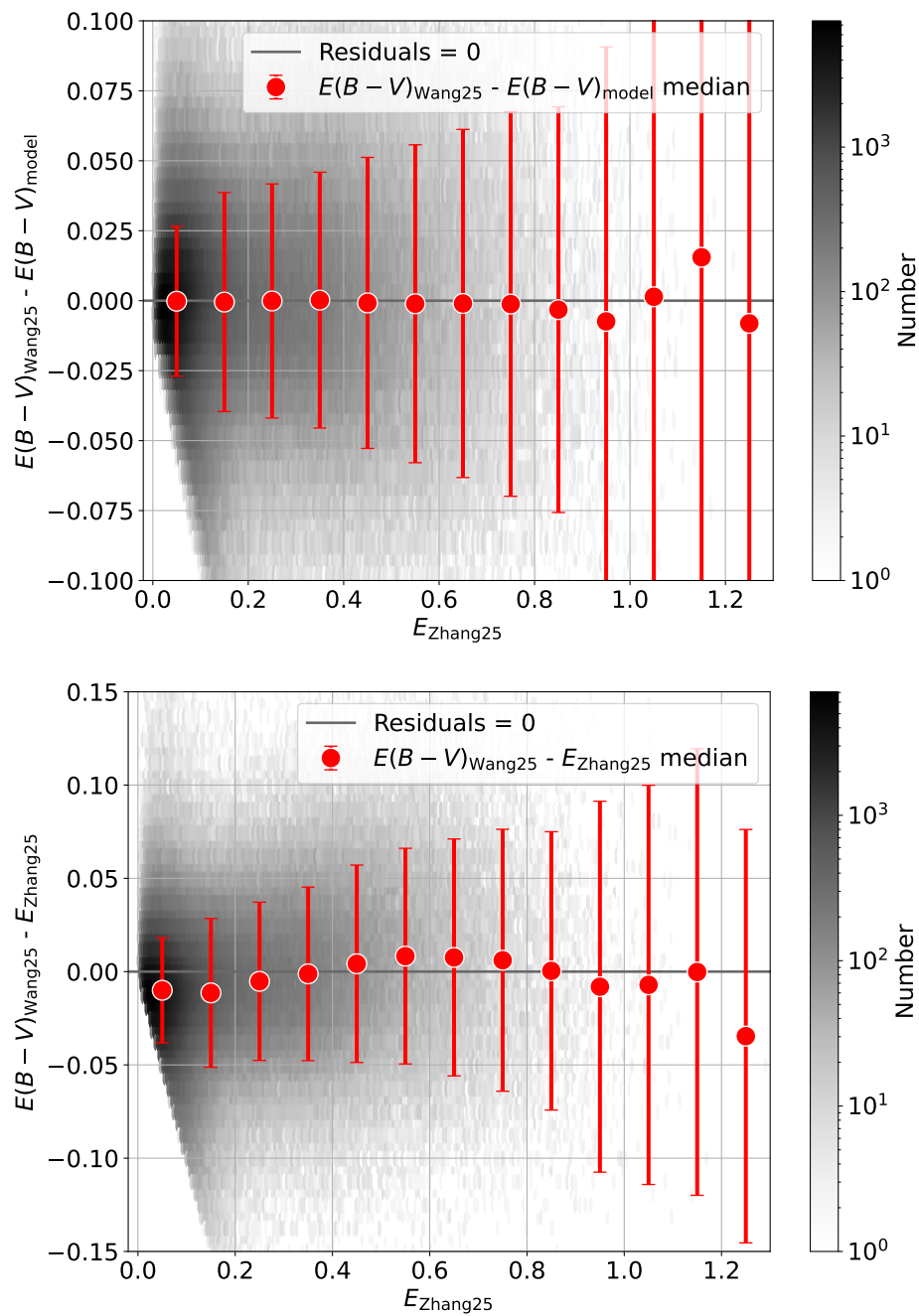


Figure 15. Median residuals and density distributions of the target $E(B - V)_{\text{Wang25}}$ relative to the model prediction $E(B - V)_{\text{model}}$ in the upper panel and to E_{Zhang25} in the bottom panel, as a function of the extinction.

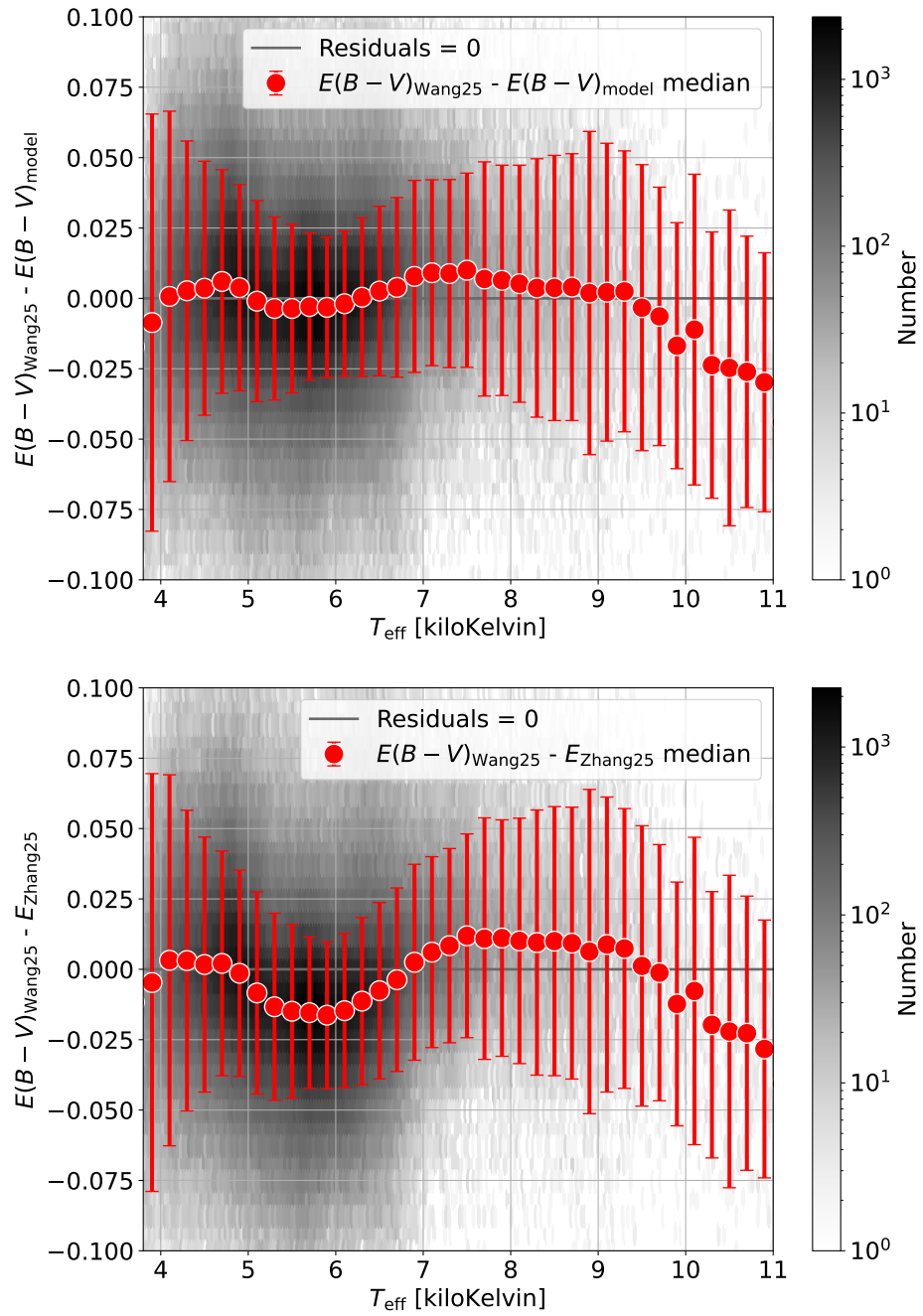


Figure 16. Same as Fig. 15, but as a function of the effective temperature T_{eff} .

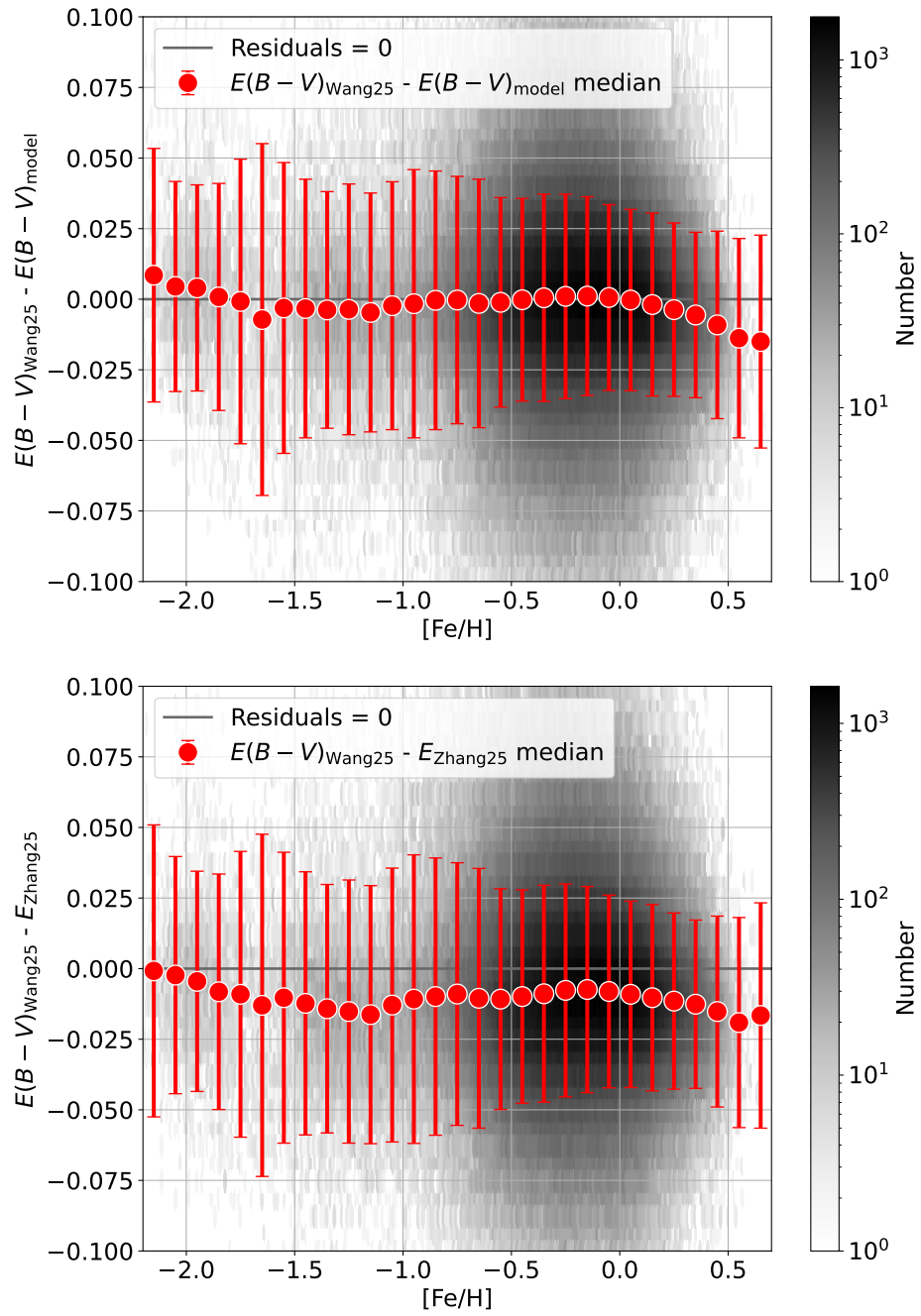


Figure 17. Same as Fig. 15, but as a function of the metallicity $[Fe/H]$.

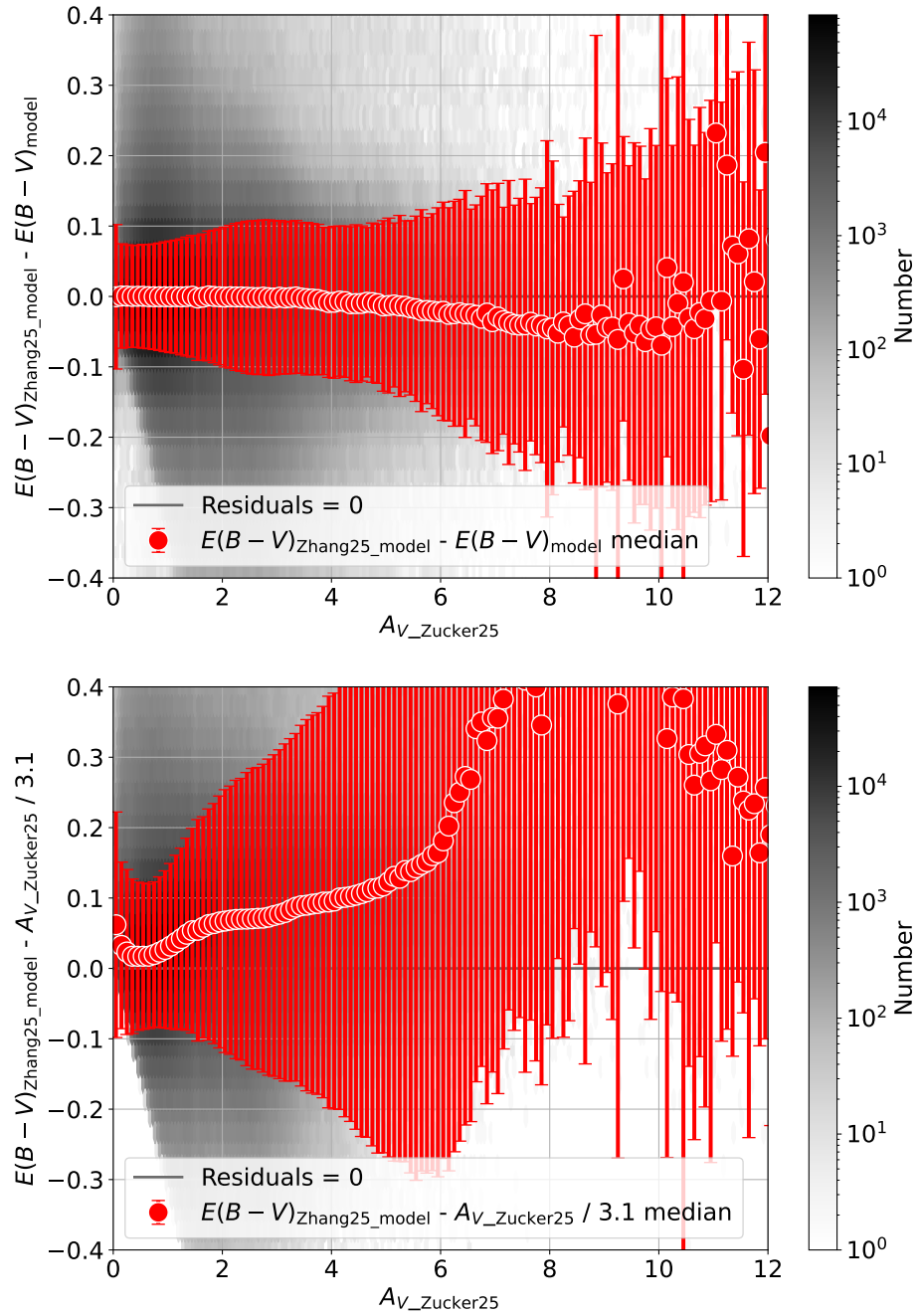


Figure 18. Median residuals and density distributions of the target $E(B - V)_{Zhang25_model}$ relative to the model prediction $E(B - V)_{model}$ in the upper panel and to $A_{V_Zucker25}/3.1$ in the bottom panel, as a function of $A_{V_Zucker25}$.

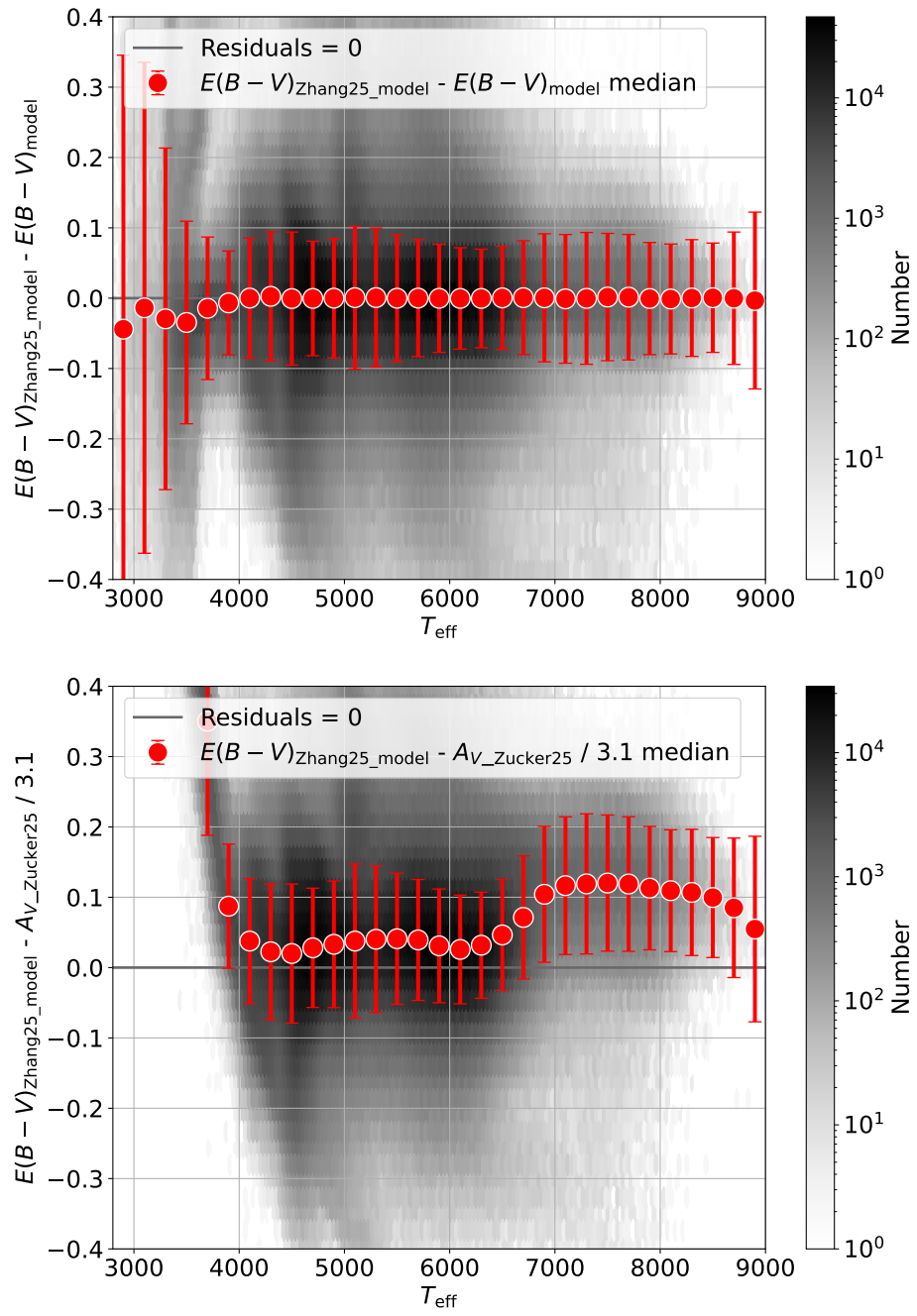


Figure 19. Same as Fig. 18, but as a function of the effective temperature T_{eff} .

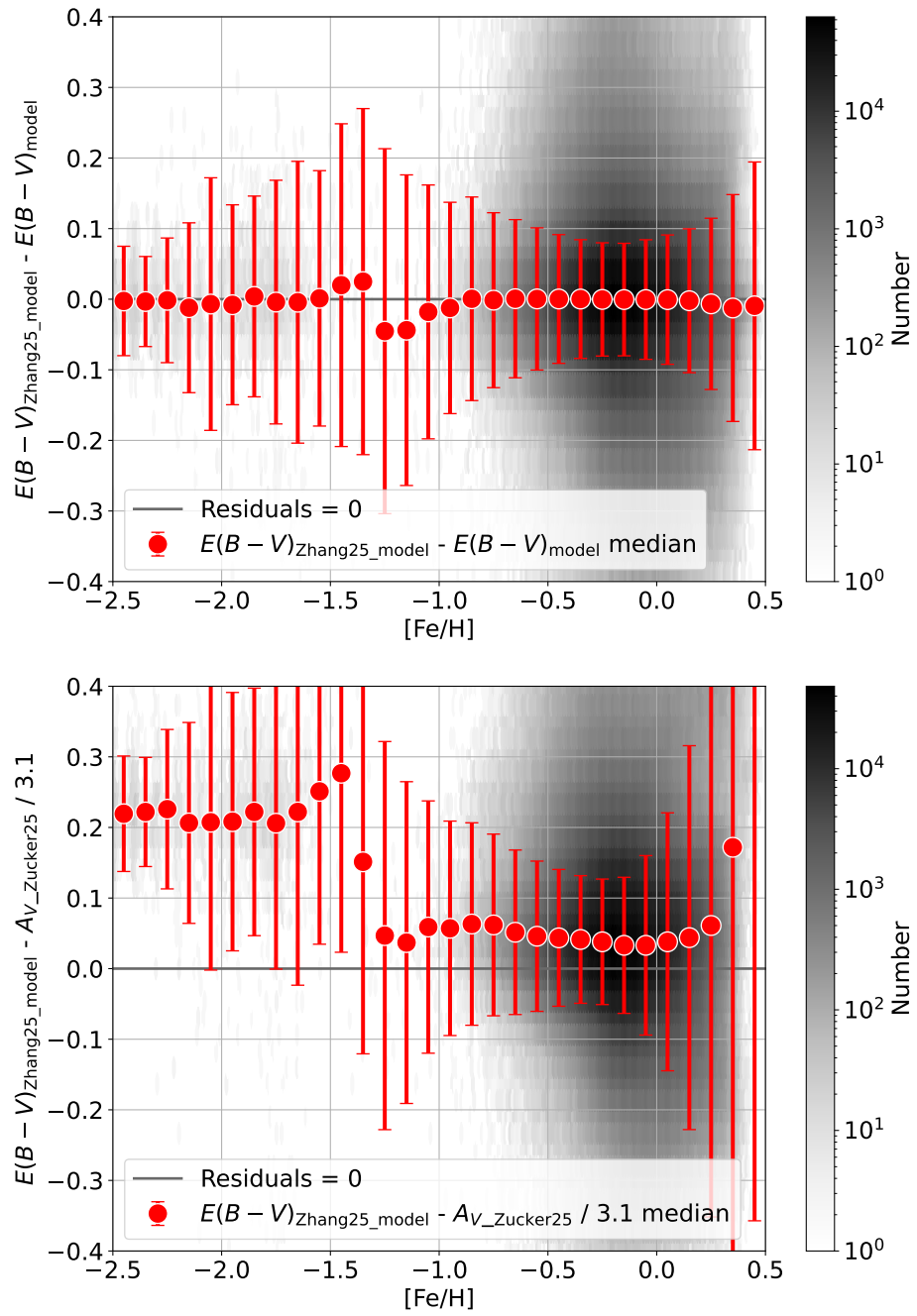


Figure 20. Same as Fig. 18, but as a function of the metallicity $[Fe/H]$.

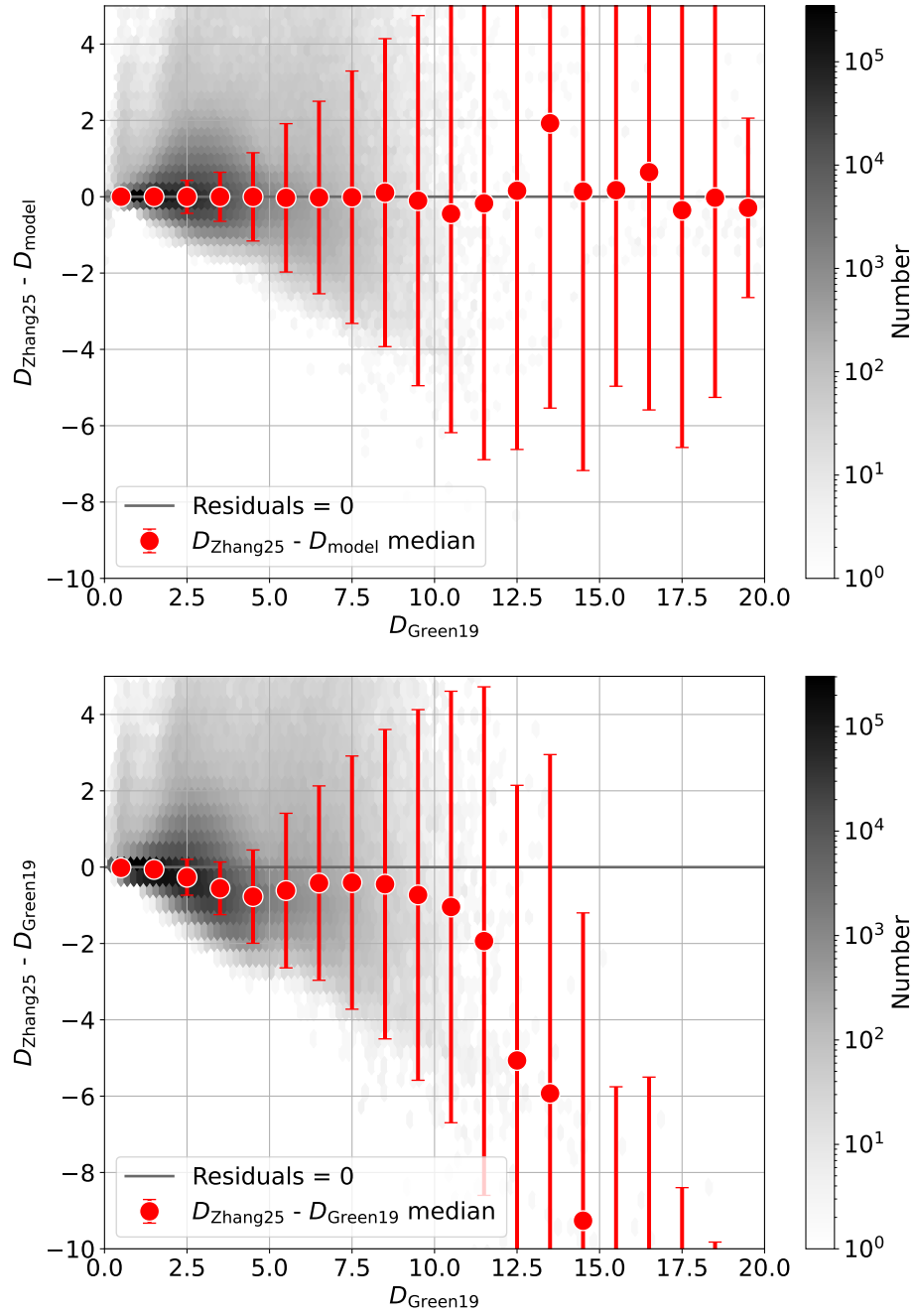


Figure 21. Median residuals and density distributions of the target D_{Zhang25} relative to the model prediction D_{model} in the upper panel and to D_{Green19} in the bottom panel, as a function of D_{Green19} . The data are grouped by D_{Green19} in intervals of 1 kpc.

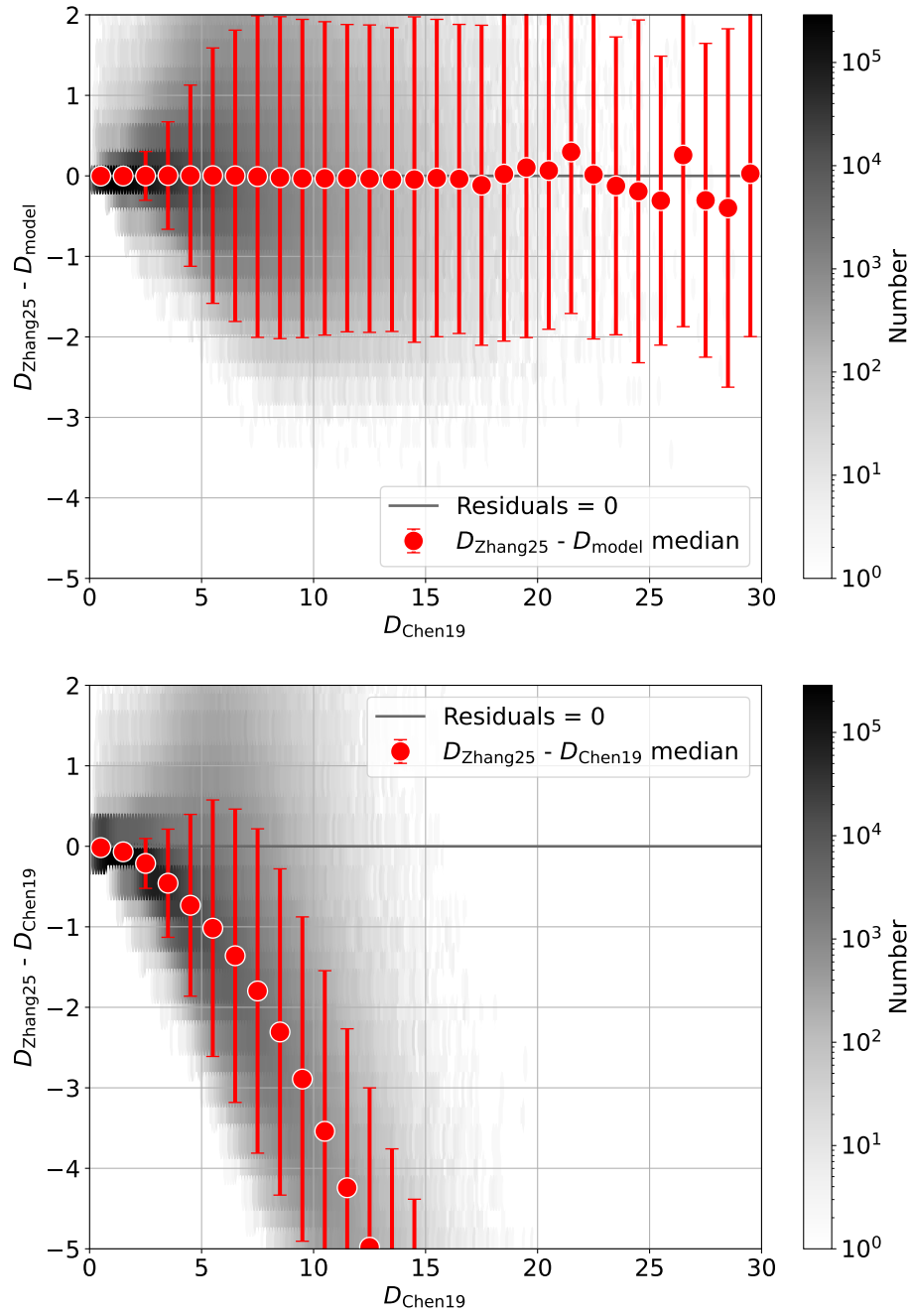


Figure 22. Same as Fig. 21, but for the distance systematics correction of Chen19.

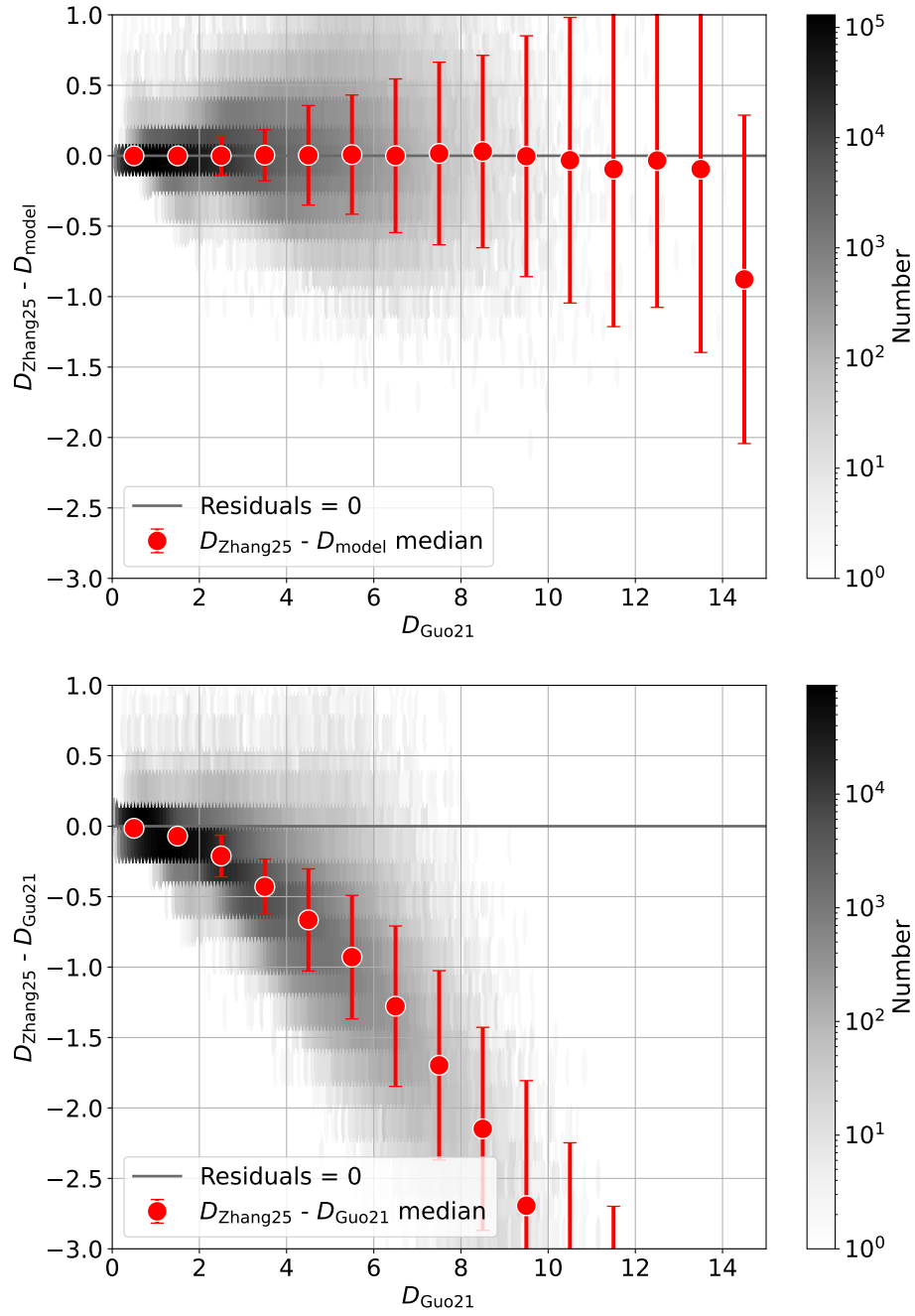


Figure 23. Same as Fig. 21, but for the distance systematics correction of Guo21.

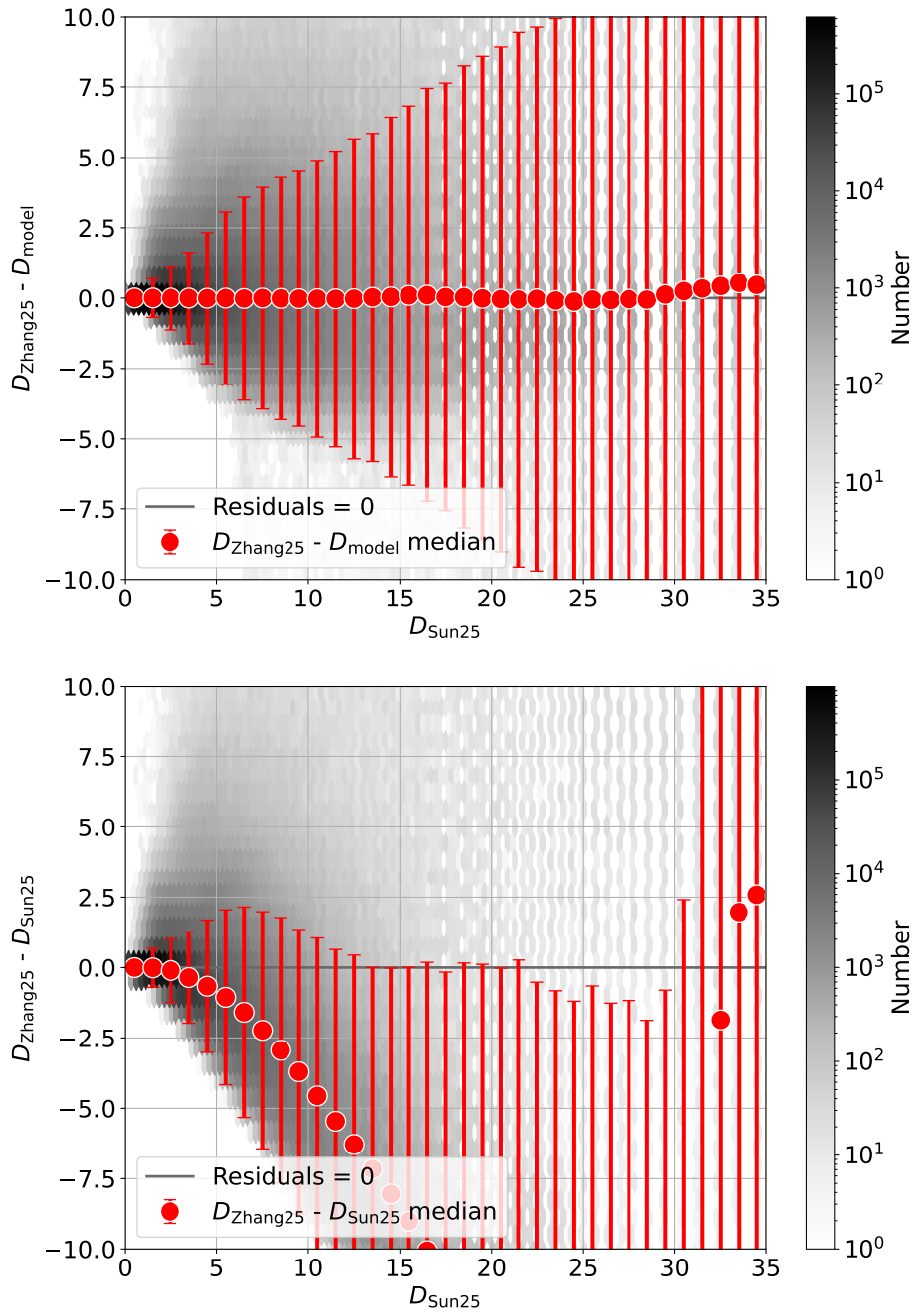


Figure 24. Same as Fig. 21, but for the distance systematics correction of Sun25.

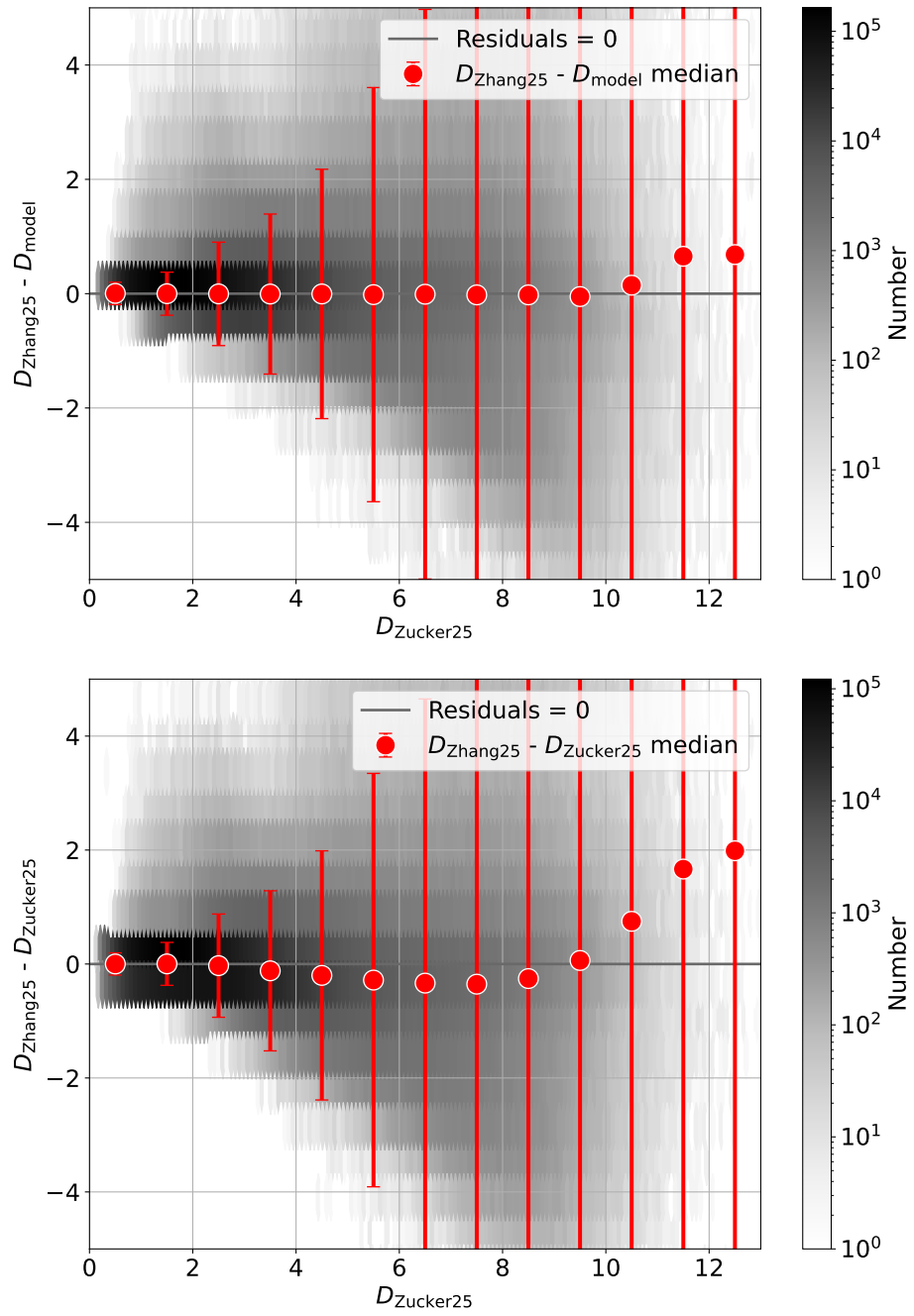


Figure 25. Same as Fig. 21, but for the distance systematics correction of Zucker25.

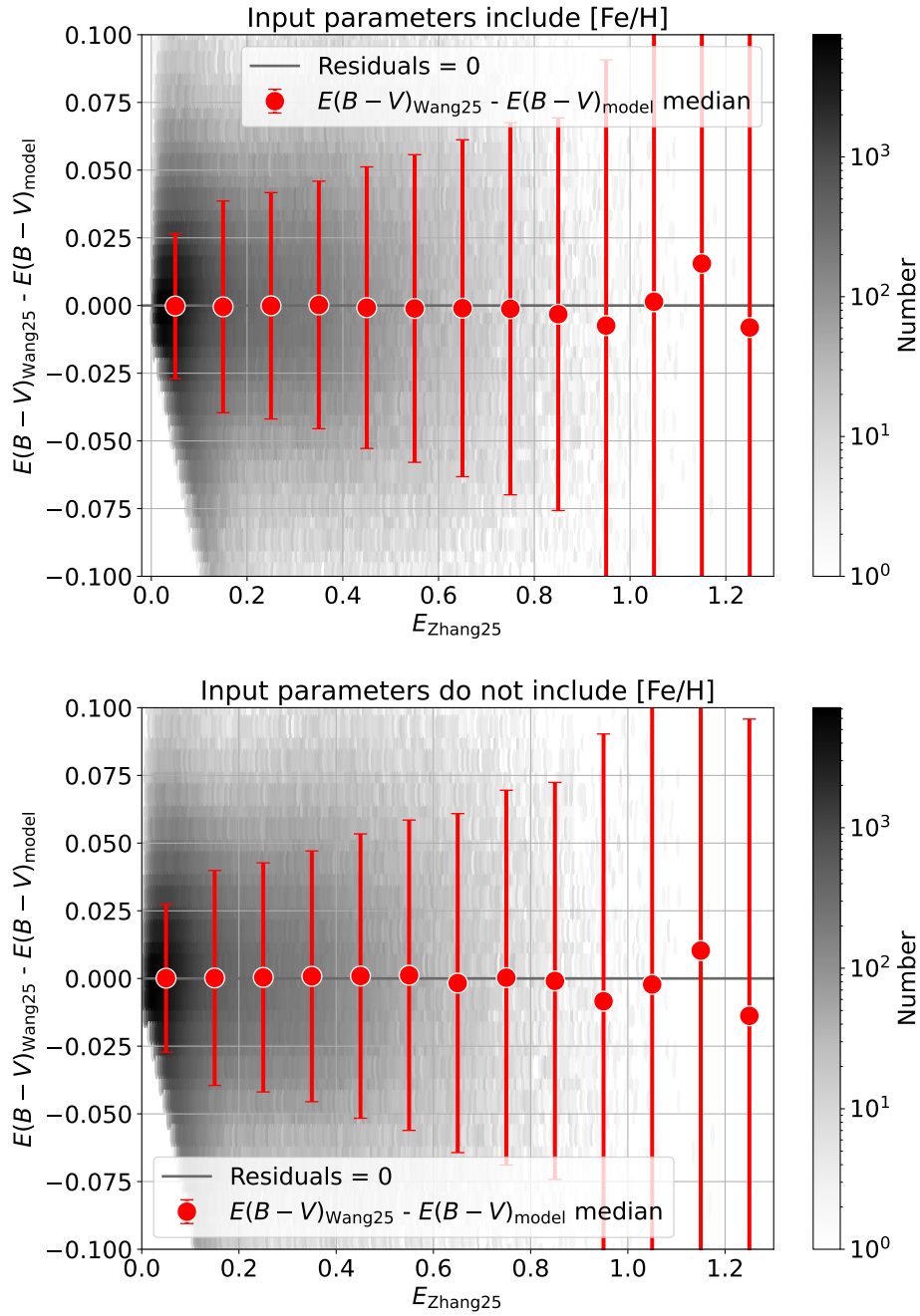


Figure 26. Median residuals and residual density of the target $E(B-V)_{\text{Wang25}}$ relative to the $E(B-V)_{\text{model}}$ obtained with and without [Fe/H] among the inputs, as a function of the extinction E_{Zhang25} .